Montanuniversity Leoben

Influence of Thermal Processing on Microstructure, Strength and Ductility of Steels for Cold Heading Applications

Masterthesis

Bernd Pfleger

This thesis was conducted at the Materials Center Leoben Forschungs GmbH in cooperation with voestalpine Wire Rod GmbH.

Leoben, 07.12.2017

The current work was carried out in the framework of the project COMET Projekt A 2.31 "Cold heading wires".

Eidesstattliche Erklärung:

Ich erkläre an Eides statt, dass diese Arbeit selbstständig verfasst, andere als die angegebenen Quellen und Hilfsmittel nicht benutzt wurden und ich mich auch sonst keiner unerlaubten Hilfsmittel bedient habe.

Affidavit

I declare in lieu of oath, that I wrote this thesis and performed the associated research myself, using only literature cited in this volume.

Leoben, 07.12.2017

_____

(Bernd Pfleger)

Acknowledgement

I would like to express my appreciation to ao. Univ. Prof. Dipl.-Ing. Dr.mont. Reinhold Ebner, managing director of the Materials Center Leoben (MCL), for the assessment of my thesis.

It gives me great pleasure in acknowledging my supervisor Dr. Marina Gruber for the support, remarks and engagements through the learning process of this thesis.

I am indebted to my many colleagues who shared willingly their precious time for informative discussions as well as all employees who were supporting me during my thesis.

In addition, a thank to voestalpine Wire Rod GmbH for providing the topic and the specimen material.

Heartfelt thanks to my girlfriend Kerstin, who is supporting me in all stages of life and keeping me harmonious.

I would like to thank my Family for supporting me during my studies and companionship through the journey of life.

Abstract

Third generation advanced high strength steels (AHSS) provide a good combination of cost reduction and favorable mechanical properties. Whilst low costs are obtained owing to the lack of alloying elements, the mechanical properties are achieved by adjusting the microstructure with thermal treatments. Particularly promising are quenching and partitioning (Q&P) processes as well as bainitic heat treatments as they optimize both, strength and ductility due to stabilization of reverted austenite.

The goal of this master thesis is to apply the fundamentals of Q&P and bainitic heat treatments on two steels that differ mainly in carbon and silicon content to obtain a combination of extremely high elongations at fracture at relatively high yield and tensile strength values. Furthermore, fractions of retained austenite at room temperature of both steels obtained by thermal processing should be compared.

To specify suitable parameters for Q&P or bainitic heat treatments the cooling behavior of the two steels is analyzed by simulation with JMatPro and dilatometry. Additionally, for the characterization of the cooling behavior, the microstructure is determined by optical methods. According to the obtained data, various Q&P and bainitic heat treatments are chosen to vary phase fractions of austenite, martensite, bainite and ferrite as well as strength and ductility. Thermal treatments of specimens are applied in dilatometer. Etching according to Klemm and Nital is used to distinguish microstructural phases. Furthermore, the fractions of austenite are detected by X-Ray diffraction. Mechanical properties are determined by hardness measurements and tensile testing values.

It is shown that the variation of Q&P parameter enables the achievement of a combination of high strength with low ductility and nearly the same fractions of retained austenite. Bainitic heat treatments with isothermal holding or continuous cooling lead to a combination of relatively high strength and ductility comparable to that of third generation AHSS. Furthermore, it can be shown that the steel with higher silicon content results in significant higher fractions of retained austenite.

Kurzfassung

Advanced High Strenght Steels (AHSS) der dritten Generation verbinden Kostenreduktion mit der Möglichkeit gezielt mechanische Eigenschaften einzustellen. Während geringe Kosten durch das Fehlen von teuren Legierungselementen entstehen wird das Werkstoffverhalten durch Veränderung der Mikrostruktur mittels thermischer Behandlung eingestellt. Besonders Quenching und Partitioning (Q&P) Prozesse sowie bainitische Wärmebehandlungen bieten eine Möglichkeit Festigkeit und Duktilität durch die Stabilisierung von Restaustenit zu verbessern.

Das Ziel dieser Diplomarbeit ist es durch Anwendung von Q&P Prozessen und bainitischen Wärmebehandlungen, angewendet auf zwei Stähle die sich wesentlich im Kohlenstoff und Silizium Gehalt unterscheiden, sowohl hohe Festigkeit als auch hohe Duktilität einzustellen. Des Weiteren sollen die Anteile an Austenit bei Raumtemperatur, generiert durch die thermischen Behandlungen der zwei Stähle verglichen werden.

Um Parameter für Q&P oder bainitische Wärmebehandlungen wählen zu können, wird das Abkühlungsverhalten der zwei Stähle mittels Simulation in JMatPro und Dilatometrie, sowie die Mikrostruktur mittels optischen Methoden festgestellt. Die Ergebnisse dienen zur Auswahl geeigneter Wärmebehandlungen, um Anteile an Restaustenit, Martensit, Bainit und Ferrit, sowie Festigkeit und Duktilität zu variieren. Die ausgewählten Q&P und bainitischen Wärmebehandlungen werden im Dilatometer durchgeführt. Klemm- und Nitalätzungen ermöglichen eine Unterscheidung der Phasenanteile in der Mikrostruktur. Des Weiteren werden die Phasenanteile des Restaustenits mittels Röntgendiffraktometrie (XRD) genauer ermittelt. Die Bestimmung der mechanischen Eigenschaften erfolgt durch Härtemessungen und Zugversuche.

Die Ergebnisse zeigen, dass die Variation von Q&P Parametern hohe Festigkeit mit geringer Duktilität und ähnlichem Gehalt an Restautenit bewirken. Bainitische Wärmebehandlungen mit isothermem Halten oder kontinuierlichem Abkühlen erzielen eine gute Kombination aus hoher Festigkeit und Duktilität und erreichen Werte der dritten Generation AHSS. Des Weiteren weist der Stahl mit höherem Silizium Gehalt höhere Anteile an Restaustenit auf.

Table of Content

List of Abbreviations and used Symbols

f_{CPE}^{γ}	amount of austenite
x_C	diffusion path for carbon
$\chi_{C_{CPE}}^{\gamma}$	carbon concentration in austenite at CPE
χ_C^{γ} , χ_C^{α}	mole fractions of carbon in austenite and ferrite
χ_C^{alloy}	entire carbon content
A	elongation at fracture
Ac_1	austenite to pearlite eutectoid transformation
Ac_3	austenitization temperatures
Acm	temperatures where cementite ejects from austenite in the hypereutectoid alloy
AFP	precipitation hardening ferritic pearlitic steel
Ag	uniform elongation
AHSS	advanced high strength steel
bcc	body centered cubic
bct	body centered tetragonal
Bf	bainite finish temperature
Bs	bainite start temperature
CCE	constrained carbon equilibrium
CCT	continuous-cooling-transformation
CPE	constrained paraequilibrium
d	diameter
D	diffusion coefficient
D_0	diffusion constant
EBSD	electron back scattered diffraction
fcc	face centered cubic
fm	fraction of austenite, which transforms to martensite
HRC	hardness according to Rockwell C
HV	hardness according to Vickers
ICF	intercritical ferrite
Mf	martensite finish temperature
Ms	martensite start temperature
Mσ	stress assisted martensite start temperature
PT	partitioning temperature
Pt	partitioning time
Q	energy barrier

Q&P	quenching and partitioning
QR	quenching rate
QT	quenching temperature
R	universal gas constant
R_m	tensile strength
$Rp_{0.2}$	0.2 % proof stress
RT	room temperature
SEM	scanning electron microscopy
T	temperature
T_A	annealing temperature
t_A	holding time at austenitization temperature
t_h	holding before reheating
TTT	time-temperature-transformation
$\dot{t}_{cool}$	velocity of continuous cooling
$\dot{t}_{end}$	coolingrate to RT
$\dot{t}_{heat}$	heating rate
$\dot{t}_{reheat}$	reheating rate
$f_{\alpha'}$	fraction of martensite
wt%	weight percent
XRD	X-Ray diffraction
Z	reduction of area at fracture
α	ferrite
α'	martensite
α_b	bainite
γ_{ret}	retained austenite

1 Introduction

Constantly increasing demands on strength and ductility of steels play an essential role in steel industry. In engineering disciplines, strength of a material is defined as the mechanical resistance against plastic deformation. The tensile strength (Rm)represents the maximum stress a material can resist [1]. Ductility is defined as the material's ability to endure plastic deformation before fracture. However, the ductility is not clearly defined by a characteristic value. The elongation at fracture (A) enables a representation of the ductility. Furthermore, the uniform elongation (Ag) and the reduction of area at fracture (Z) are possibilities to describe ductility. These values are not identical and not directly comparable [2].

A group of steel types and grades, which provide high strength and high ductility are called advanced high strength steels (AHSS).
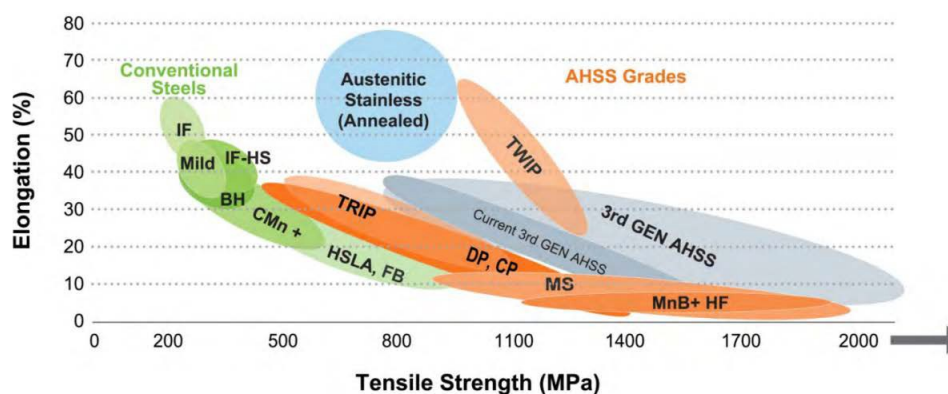

Fig. 1: Ashby Map representing the strength–ductility relationship of various conventional and AHSS grades **[3]**

Fig. 1 gives an overview of AHSS grades and conventional steel grades. It is evident that AHSS grades are broadly spread. Thus, AHSS are subdivided in first, second and third generation AHSS. Dual – phase steels (DP), transformation induced plasticity steels (TRIP), complex – phase steels (CP) and martensitic steels (MS) belong to the group of first generation AHSS. The second generation is characterized by an austenitic phase, stable at room temperature (RT) with high Mn (17 – 24%) and sometimes Al content. A typical representative is the twinning induced plasticity steel (TWIP). The focus of this diploma thesis lies on third generation AHSS. Their characteristics exceed those of first generation AHSS without the full costs of stabilizing elements. Desired properties are achieved by appropriate thermal treatments, e. g. for quenching and partitioning steels (Q&P). The strength and ductility of

these steels is optimized by the variation of fractions of martensite and retained austenite (γ_{ret}) [3, 4].

The retained austenite is stabilized by partitioning of carbon. Hence, diffusion plays a major role in Q&P processes. The mean diffusion path of an atom according to the random walk model is the diffusion path x and can be calculated with Equ. 1. The diffusion path is dependent on the diffusion coefficient D and time t [5].

$$x = 2\sqrt{Dt}$$ (Equ. 1)

The diffusion coefficient in solid materials is calculated by Equ. 2 [6]. The diffusion constant, the energy barrier (J·mol^{-1}), which needs to be exceeded for diffusion, the universal gas constant (J·K^{-1}mol^{-1}) and the temperature (K) are indicated by D_0, Q, R, T, respectively [7].

$$D = D_0 * \mathrm{e}^{-\frac{Q}{RT}}$$ (Equ. 2)

The enrichment of carbon in austenite by diffusion impedes the decomposition of austenite into ferrite and cementite as well as the martensite formation and the stress induced martensitic transformation [8, 9].

This thesis concentrates on the optimization of strength and ductility by Q&P processes and bainitic heat treatments (also termed as austempering in literature [10]), where the stabilization of austenite plays a major role. Therefore, knowledge of the transformation kinetics during cooling to specify suitable parameters for thermal treatments are obtained by analyzing the material behavior by means of simulation with JMatPro and dilatometry as well as microscopic phase analysis. The combination of different etching methods (colour etching according to Klemm and etching with Nital) for microstructural characterization offers an opportunity to distinguish phase fractions.

Specimens are treated in dilatometer, as Q&P and bainitic heat treatments demand complex temperature control. To this end, fractions of austenite, martensite, bainite and ferrite are varied to increase strength and ductility. Furthermore, fractions of austenite are detected with X-Ray diffraction. Hardness measurements and tensile testing provide values for characterization of mechanical properties.

2 Morphological Structures in Steels and Conventional Heat Treatments

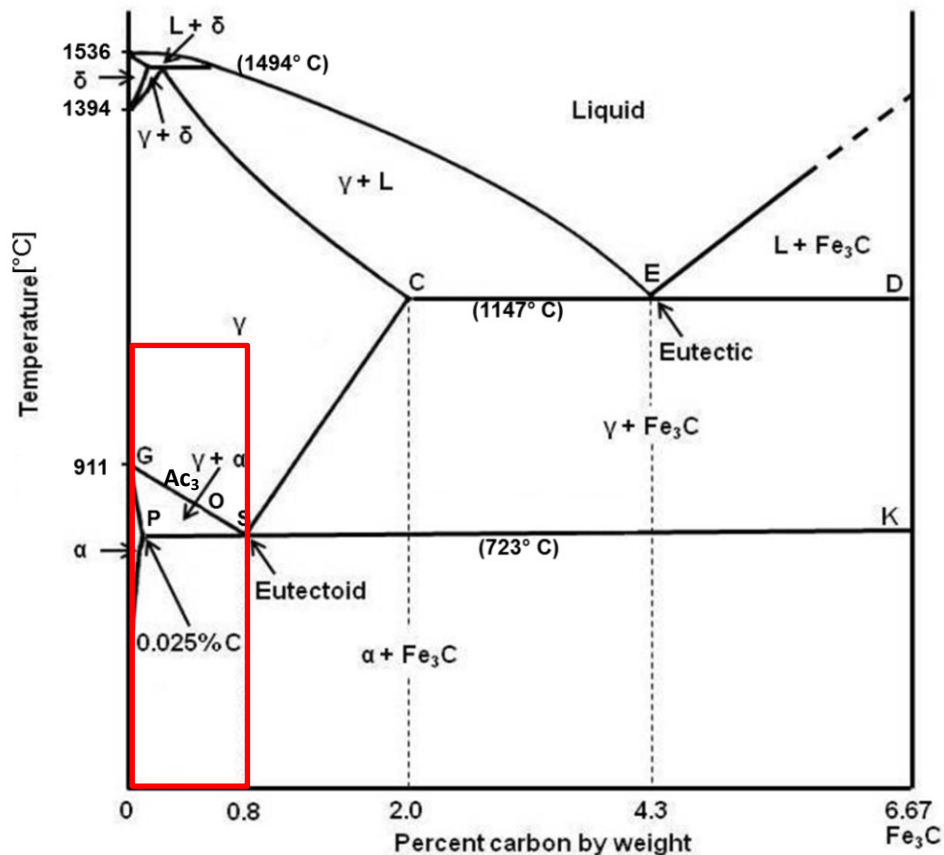## 2.1 Phase Diagram and Equilibrium Phases

Fig. 2: Iron-carbon equilibrium diagram. L, δ, γ, α, Fe_3C indicate liquid, δ-ferrite, austenite, α-ferrite and cementite [11].

A tool to gain a fundamental knowledge about possible phase formation during heat treatment is the iron – carbon equilibrium diagram or the metastable iron – iron carbide diagram shown in Fig. 2. This diagram indicates the possible phases, which may appear in equilibrium at constant pressure, if carbon is the only alloying element. Critical lines in the binary phase diagram are characterized by a significant observable phase transformation. As for this work the concentration is put on Q&P and bainitic heat treatments, only carbon contents lower 0.8% as well as temperatures below 1000°C are of interest. Thus, the following paragraph focuses on the marked region of the phase diagram. Austenite is stable above the G, O, S line, i.e. Ac_3. At temperatures below this line austenite (γ) and ferrite (α)

are present. The P, S, K line, i.e. Ac_1, represents the temperature of austenite to pearlite eutectoid transformation. Below this temperature no austenite exists in equilibrium [12]. Compositions with carbon content lower than 2.06 wt% are termed as steel, whereas compositions with more carbon, are designated as cast iron. Predicted phases for steel according to the iron carbon equilibrium diagram are ferrite, cementite, austenite and pearlite.

Ferrite

The crystal structure of ferrite is body centered cubic (bcc) with a packing density of 68 % calculated from the unit cell. The elongation at fracture and the reduction of area at fracture of ferrite is around A = 50% and Z = 80% [13]. Ferrite is soft with about 150 HV (hardness according to Vickers) [14] and highly corrodible. Ferrite is subdivided in δ and α ferrite depending on temperature (see Fig. 2).

Cementite

Cementite is a compound of iron and carbon in the form of the iron carbide Fe_3C. It occurs as metastable phase in steel and cast iron. This phase belongs to the group of the Häggs phases [15]. The unit cell is rhombohedral and its hardness is around 800 HV. Cementite is ferromagnetic and brittle [16].

Pearlite

Decomposition of 0.8 % C austenite results in pearlite formation. Pearlite consists of ferrite and cementite in alternating lamellar arrangement and is formed during cooling under Ac_1 in the iron – carbon equilibrium diagram. The strength of pearlite depends on interlamellar spacing. Fracture toughness and tensile ductility are invers proportional to the former austenite grain size. The yield strength ($Rp_{0.2}$) of pearlite is around $Rp_{0.2}$ = 550 MPa and hardness according to Rockwell is around HRC = 25 [17].

Austenite and its Stabilization

Austenite has a homogeneous microstructure and is represented by γ. The packing density is 74% resulting from the face centered cubic (fcc) crystal structure. Austenite is usually not stable at room temperature. Due to the higher packing density of austenite in comparison to ferrite, a contraction of volume will appear during phase transformation by heating above Ac_1. Typical values of tensile strength and 0.2% - yield strength are R_m = 600 MPa and $Rp_{0.2}$ = 200 MPa. Thus, the formability of austenite is very high. It is paramagnetic and has low corrosion susceptibility [16, 18].

Austenite, which results from an incomplete transformation to martensite or bainite, i.e. retained austenite, plays an important role for Q&P or bainitic steels. This retained austenite is located within a martensitic matrix in from of blocks or films.

Austenite can be stabilized by alloying with elements, which expand the austenite region of the iron carbon equilibrium diagram (see chapter 4 "Influence of Alloying Elements"). In particular, an enrichment of interstitials like nitrogen and carbon in austenite impede the diffusionless transformation of austenite to ferrite during cooling and thus, stabilize the austenite [19]. Moreover, austenite morphology and mechanical deformation during processing, which induces dislocations via plastic deformation, effects the austenite stability. For example, Wang and van der Zwaag show that small γ grains are more stable than large ones, as the necessary nucleus density for martensitic transformation is not reached in small grains [20]. Furthermore, the stability of austenite depends on blocky, interlath lamellar, fine film, C content and grain orientation of the austenite grain. Especially, thin austenite films exhibit a stability due to the stronger enrichment with carbon. This is caused by lower necessary diffusional paths and the stabilization through strains induced during martensite growth. Thus, the probability that coarse blocks decompose into pearlite or transform to martensite is much higher than those of fine films or lamella [3, 21]. According to Bhadeshia, austenite transformation to martensite or bainite is possible if dislocation movement is not impeded by other dislocations or obstacles. Hence, high dislocation density, e. g. induced by mechanical deformation, stabilizes the austenite [22].

If conditions are changed and consequently the state of equilibrium is abandoned, other phases may occur, e. g. with increasing cooling rate fractions of bainite and fractions of martensite will appear and increase, respectively.

2.2 Bainite

Bainite is an aggregate of phases consisting of fine plates of ferrite often separated by phases such as retained austenite or cementite and is indicated by α_b in this thesis [23, 22]. Bainite is formed during accelerated cooling of austenite at temperatures between those of pearlite and martensite, i.e. 215-540°C [24].

The formation of the ferritic component is explained by a shear mechanism [25], which implies a diffusionless formation of bcc laths from austenite.

This diffusionless growth of a bcc subunit during bainite formation generates a bcc plate supersaturated with carbon. Consequently, the excess of carbon is partitioned to the surrounding austenite, as austenite has a higher solubility for carbon, or it precipitates as carbides. The next plate must nucleate and grow in carbon enriched austenite with a lower driving force as carbon stabilizes austenite [23]. Thus, transformation temperature is reduced as described by the T_0 concept in Fig.3
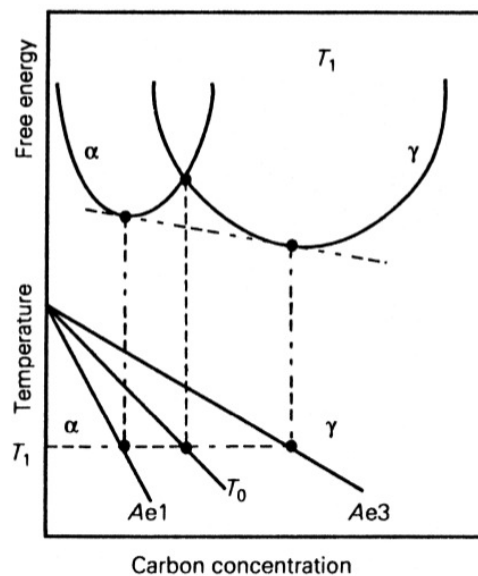

Fig. 3: T_0 concept for bainitic transformation of an Fe-C phase diagram **[26]**.

The T_0 temperature is the temperature at which bcc and fcc with same chemical compositions exhibit the same free energy [26]. The T_0 line shows the dependency of transformation temperature as a function of carbon concentration. Austenite with a carbon concentration on the left side of the T_0 line can transform without diffusion to bcc, as the free energy of bcc is lower than the free energy of fcc. Whereas, a transformation to bcc is not possible if T_0 is exceeded. Ae3 represents the temperature dependence of carbon concentration on the phase fields of fcc and fcc + bcc. Thus, according to the T0 line the

diffusionless transformation of fcc to bcc stops long before the carbon concentration reaches Ae3 [22, 26, 27]. Beside the carbon enrichment mentioned above, austenite is stabilized by plastic deformation. The bainitic transformation induces strains through the change in volume. The strain energy of the bcc subunits in bainite is about 400 J mol^{-1} [23]. As a result of these strains, the surrounding austenite is deformed and thus transformation of the bainite lath stops. For further transformation another bainite lath must be nucleated. To sum up, the size of a bainite lath depends on a balance between the strain energy and carbon enrichment in austenite. Hence, bainite consists of small platelets, which are conjuncted in a sheaf. This property is a unique feature of bainite [22, 26].

T_0 corresponds also to the bainite start temperature (Bs) for an alloy with a distinct carbon content and thus, Bs is defined as the highest temperature at which bainitic transformation can occur and is approximately calculable with Equ. 3. It is the Steven & Haynes' formula using isothermal transformation diagrams determined for low and high alloy steels [28]. More equations for determination of Bs are listed in "Steel Forming and Heat Treating Handbook" by Gorni [29].

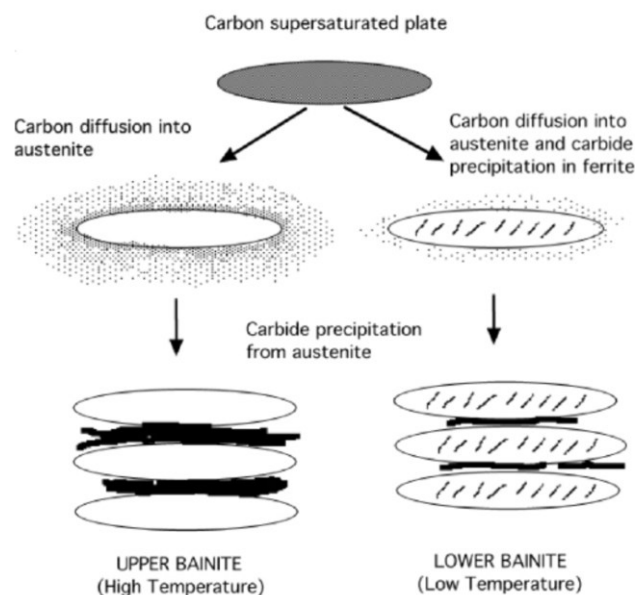$$B_s = 656 - 57.7C - 35Mn - 75Si - 15.3Ni - 34Cr - 41.2Mo \qquad \text{(Equ. 3)}$$

Fig. 4: Development of upper and lower bainite **[27]**.

The subdivision into upper and lower bainite is indicated by Fig. 4. The nature of bainite depends on temperature. Upper bainite forms at higher temperatures in the range of 550 - 400°C where the excess carbon partitions into austenite and stabilizes it. Furthermore, some carbon forms elongated carbides at the boundaries between the ferrite subunits. At the

lower temperature range between 400 – 250°C, the impeded diffusion during lower bainite formation provides an opportunity for some carbon to precipitate as fine carbides in the bainitic ferrite plate. The carbon in the austenite behaves like in upper bainite. Accumulations of bainitic-ferrite plates are called sheaves and appear on macroscopic scale in the form of wedge - shaped plates [26, 30, 27]. Alloying can suppress the carbide formation (see chapter 4).
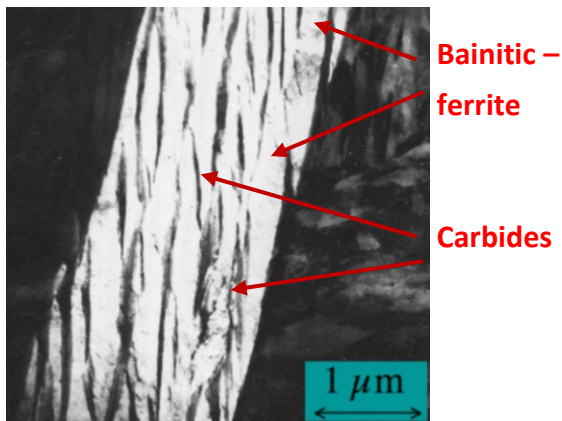

Fig. 5: Upper bainite with cementite between ferritic plates, picture obtained by TEM [31].
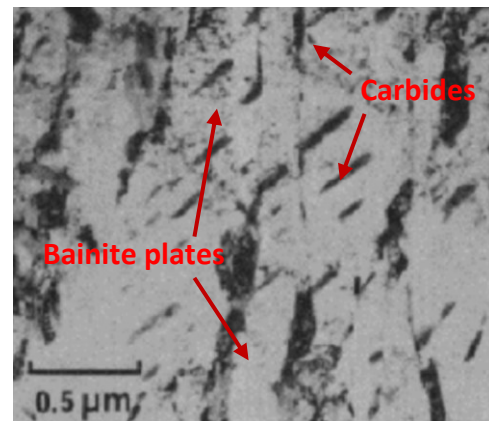

Fig. 6: Lower bainite with carbide precipitations in the ferrite lath, picture obtained in TEM [31].

Upper bainite is depicted by Fig. 5 with the characteristic bainitic ferrite lath, which are surrounded by elongated carbides. Fig. 6 shows lower bainite with carbon precipitated as carbides in the bainitic ferrite platelets as well as between the platelets.

The change in lattice of austenite to bainite transformation is caused by a transfer of atoms across the interface for which glissile and sessile interfaces play important roles.
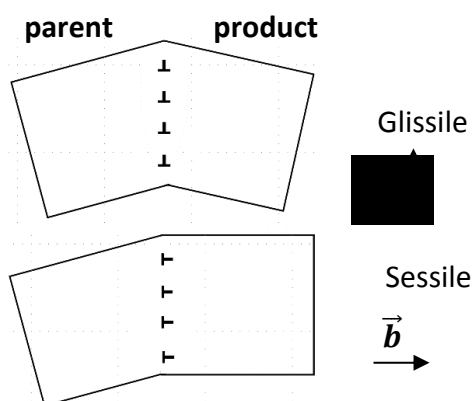

Fig. 7: Glissile and sessile interfaces consisting of dislocation arrays, $\vec{b}$ is the Burgers vector [22].
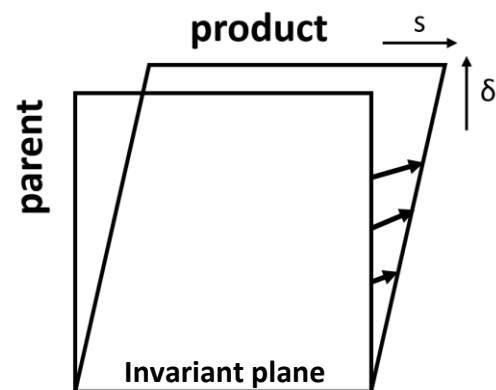

Fig. 8: Shape deformation via an invariant plane strain, where the shear component of the displacement strain is indicated by s and the dilatation component by δ. [22, 26].

Fig. 7 demonstrates the interfaces for parent (e.g. austenite) and product (e.g. bainite) crystals. The difference between sessile and glissile interfaces is explained by the Burgers vector. The Burgers vector of the dislocations of an glissile interface lies outside of the plane boundary. Thus, sessile interfaces would need to climb by diffusion and glissile interfaces not [22]. Hence, diffusionless transformation can only occur if glissile interfaces are present. Any obstacle such as dislocations generated by plastic deformation of austenite of the parent phase or carbides would hamper the movement of glissile interfaces. This limits the scale of ferritic plates during bainite formation and is the reason why a bainite plate does not divide the whole austenite grain [30]. The transformation of austenite results in an increase in volume and induces shape deformation as shown in Fig. 8. The horizontal plane, denoted as invariant plane, is neither rotated nor distorted. Whereas, the displacement strain consists of a shear component (s), parallel to the invariant plane and a dilatation component (δ), normal to it. As the transformation of the crystal is impeded in expansion by surrounding crystals, large displacements are not possible as mentioned before. To reduce elastic strains the plate is formed in the shape of a lens (lenticular), whereby the displacement at the tip itself is insignificant [22, 26].

2.3 Iron - Carbon Martensite

Martensite forms rapidly through accelerated cooling under a certain temperature out of austenite and is indicated by α'. Thereby, the face centered cubic crystal structure of austenite transforms by cooperative atomic movement (shape deformation) to a bct or bcc lattice of martensite, where the tetragonality depends on carbon content. Thus, a fundamental requirement of martensite is that the transformation is fully diffusionless and no chemical decomposition takes place. Therefore, even no diffusion of interstitial elements is present during transformation, as the velocity of transformation is way faster as the movement of atoms [32].
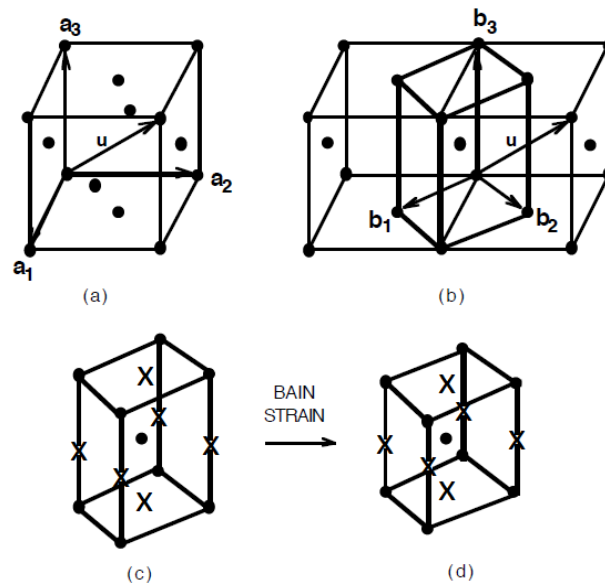
Fig. 9: Theoretical model of martensite transformation, where (a) demonstrates an fcc unit cell. (b) Relationship between the fcc and bct unit cells in austenite. (c) – (d) Deformation of the bct cell of austenite via Bain Strain into a bcc martensite lattice. The axes of the bct cell are indicated by b_1, b_2 and b_3. Positions of carbon in the unit cell are marked with x [33].

Fig. 9 demonstrates the emergence of martensite without any carbon content, where Fig. 9 (a) represents the fcc unit cell of austenite. Two fcc unit cells with a bct cell, elongated in the b_3 direction, are shown in Fig. 9 (b). A certain strain, the "Bain Strain" needs to be applied for cubic martensite transformation. As shown in Fig. 9 (c) - (d) the b_3 axis undergoes a compression and b_1 and b_2 underlie an elongation, as well as a suitable rigid body rotation. This results in an invariant plane strain, which consists of glissile dislocation and is needed to generate new surface for martensite formation [33]. The invariant plane strain is a combination of the Bain strain and a lattice invariant shear deformation such as twinning or slip, comparable with bainite formation of Fig. 8 [26].

The volume and the tetragonality of the martensitic unit cell increases with the carbon contend of the alloy, where carbon is dissolved as interstitial atoms in the octahedral sites as marked with x in Fig. 9 [9, 32, 34].

Austenite to martensite transformation starts during quenching at a certain temperature, which is termed as martensite start temperature (Ms) and progresses upon continuous cooling [32]. Martensite nucleates preferably at grain boundaries, dislocations and grows with sonic speed in metals (3000-5500 m/s [35, 36]), thereby dissecting the austenite grain into smaller pieces until the austenite is stabilized by the transformation strains due to increasing volume during transformation or it is totally transformed [32, 37]. The martensite finish temperature (Mf) represents the end of martensitic transformation.
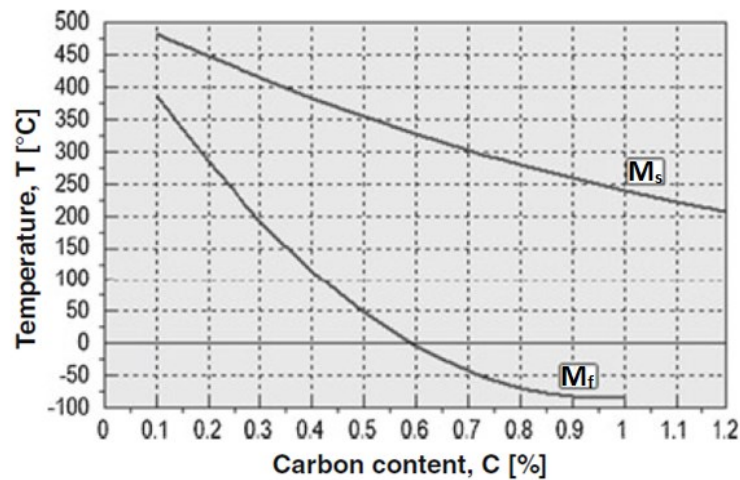
Fig. 10: Influence of carbon content to martensite start and finish temperature [38].

The martensite start and finish temperatures can be varied by alloying. Carbon has a strong effect on these temperatures, as shown in Fig. 10. Increasing carbon content leads to a decrease of transformation temperature. The influence of different alloying elements on Ms is indicated by the linear relationship of Equ. 4 [39]. The equation is based on calculations which have been done by Liu by comparison of pure iron and an ultra-low carbon alloy steel with a carbon content higher than 0.05 wt% [39]. Other possible calculations of Ms are summarized by Gorni in "Steel Forming and Heat Treating Handbook" [29].

$$Ms(°C) = 525 - 350(C - 0.05) - 45Mn - 30Cr - 20Ni - 16Mo - 5Si - 8W + 6Co + 15Al - 35(V + Nb + Zr + Ti) \quad \text{(Equ. 4)}$$

Besides alloying, martensite transformation is influenced by other mechanisms. Refinement of austenite grain size leads to Hall-Petch strengthening which results in a greater resistance to martensite formation [40]. The increase of dislocation density in the austenitic phase results in higher stability of austenite. Hence, higher dislocation density decreases Ms or even supresses the martensitic transformation [41]. Martensitic transformation does not necessarily need continuous cooling. Applying stresses or strains may induce austenite-martensite transformation. Due to this, it is possible to receive martensite at constant temperature, which is known in literature as TRIP (transformation induced plasticity) effect [9].

3 Thermal Treatments for Austenite Stabilization

3.1 Quenching and Partitioning

Quenching and Partitioning (Q&P) steels belong to the group of third generation AHSS. They are characterized by high strength and high ductility, which is mainly resulting from the microstructural combination of martensite and stabilized retained austenite [3]. This microstructural combination is achieved by a multistep heat treatment. After austenitization and quenching to a defined temperature, distinct amounts of retained austenite are stabilized during a subsequent partitioning treatment by diffusion of carbon from the martensite to austenite. For austenite stabilization during partitioning with carbon austenite decomposition must be impeded. This is conducted by alloying with Si, P, or Al, as these elements hamper cementite formation [8].

3.1.1 Processes

Q&P treatments can be divided in processes with full austenitization and processes with intercritical annealing and can be subdivided in Q&P in one step or in two steps, as shown in Table 1.

The process starts with austenitization followed by quenching to achieve a controlled amount of martensite. Annealing at temperatures above Ac_3 leads to complete transformation to austenite, whereas annealing in the temperature range between Ac_3 and Ac_1 causes a mixture of ferrite and austenite. Thus, Q&P with intercritical annealing leads to a smaller initial amount of austenite with higher initial carbon concentration. The higher initial carbon concentration is a result of early carbon partitioning from the ferrite to the austenite during intercritical holding [8, 42]. The quenching temperature is between Ms and Mf and determines the fractions of martensite and retained austenite. Generally, by increasing the quenching temperature the microstructure consists of decreasing amounts of martensite and increasing amounts of austenite [8, 42]. A high quenching rate is needed to avoid ferrite, ferrite + cementite (i.e. pearlite) and bainite [3].

The subsequent partitioning treatment is necessary to enhance the carbon diffusion to enrich the austenite with carbon and thus, to stabilize the austenite against transformation to bcc phases e.g. martensite.

Table 1: Q&P Processes.

	Full Austenitization	Intercritical Annealing
One Step		
Two Steps		

The solubility of carbon in austenite is much higher than in ferrite. This is perceivable in the iron – carbon diagram where austenite is able to ingest 2.06 wt% of carbon and ferrite can only solute 0.02 wt%. During the isothermal holding, typically around 300 - 550°C [43, 44, 45, 46], many different microstructural processes may appear. For example: isothermal martensite formation, migration of the martensite/austenite interface, transition carbide formation, carbon trapping at dislocations, cementite formation and bainite formation [4].

Q&P in one step reduces complexity of process control as the partitioning treatment is realized by isothermal holding at quenching temperature, whereas Q&P in two steps requires reheating. As carbon diffusion rises with increasing temperatures, the enrichment of carbon in austenite during partitioning process of Q&P in two steps is higher at same partitioning time comparable to Q&P in one step. In the opposite, the risk of austenite decomposition increases with increasing temperature [47, 48, 49].
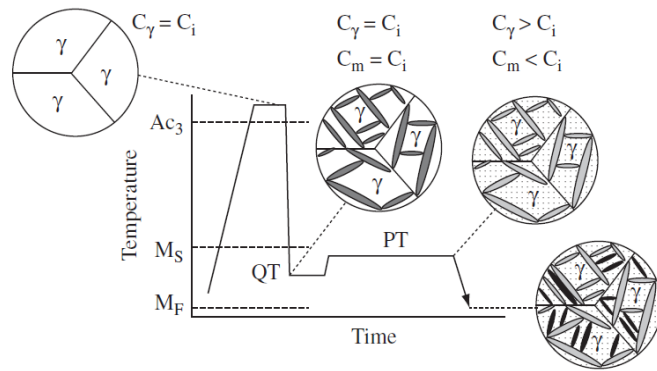
Fig. 11: Schematic illustration of the Q&P process with full austenitization. Ci, Cγ, Cm represent the carbon concentrations in the initial alloy, austenite, and martensite, respectively. QT and PT are the quenching and partitioning temperatures [8].
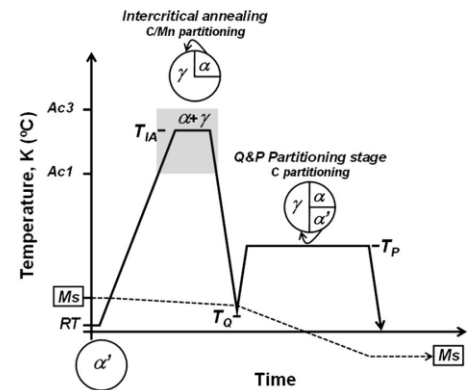
Fig. 12: Visualization of the formation of microstructure during Q&P with intercritical annealing [42].

Fig. 11 demonstrates an example of the phase formation and stabilization of austenite by carbon partitioning. After the partitioning treatment and enrichment of austenite with carbon, some untempered martensite forms during the quench to room temperature, demonstrated by the dark needles in the pattern of the microstructure [8]. The phase formation with intercritical annealing is shown in Fig. 12. As the former microstructure does not completely transform to austenite during intercritical holding, one receives ferrite in addition to martensite and retained austenite. The dotted line visualizes how the Ms temperature is lowered during partitioning time.
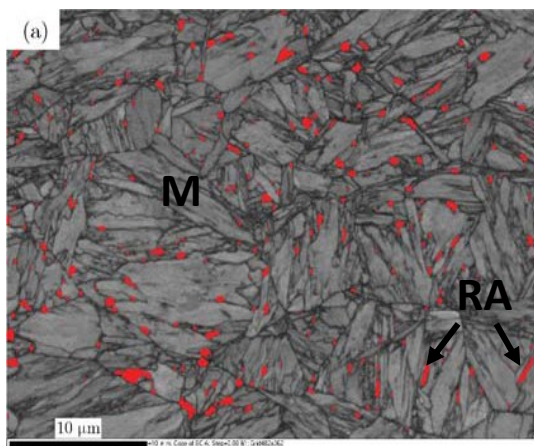

Fig. 13: EBSD image of Q&P with full austenitization. Martensite is represented by M and RA indicates retained austenite [50].
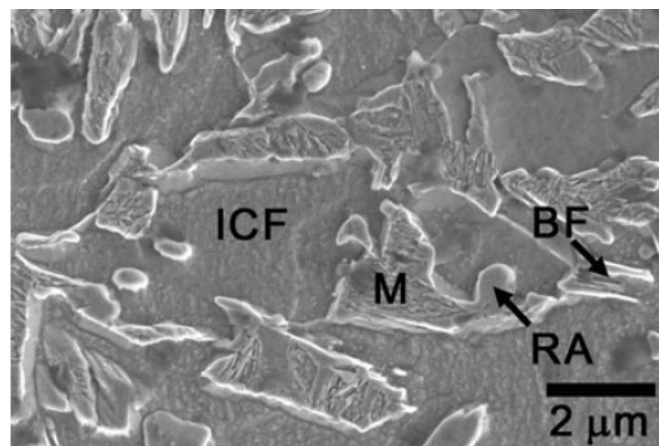
Fig. 14: SEM image of Q&P with intercritical annealing. ICF, M, RA, BF indicates intercritical ferrite, martensite, retained austenite, bainitic ferritic, respectively [51].

Typical morphological structures of fully austenitized steels after Q&P are tempered martensite laths with retained austenite and untempered martensite laths formed during final quench. Islands of bainite may also be present, depending on quenching-/partitioning-temperature and time [3]. Fig. 13 shows the microstructure of a steel with 0.2 wt% C,

1.51 wt% Si, 1.84 wt% Mn, 0.01 wt% P and 0.0052 wt% S after quenching and partitioning with full austenitization. Bright needle shaped areas in the electron back scattered diffraction (EBSD) picture are martensite-lath. Owing to the limit of EBSD resolution, only blocky and coarse austenite fractions are demonstrated in red due to face mapping [50].

The microstructure after Q&P with intercritical annealing is characterized by a ferritic matrix with islands of tempered and untempered martensite and retained austenite, as shown in Fig. 14. The scanning electron microscopy (SEM) image demonstrates the microstructural combination of intercritical ferrite (ICF), martensite (M), retained austenite (RA) and some bainitic ferritic structures (BF) after quenching and partitioning with intercritical annealing of a 0.19 wt% C, 1.59 wt% Mn and 1.63 wt% Si steel [51].

Table 2 demonstrates a variety of mechanical values from literature, which are achievable with Q&P treatments [3, 52].

Table 2: Mechanical values achievable with Q&P treatments

Composition	Rm [MPa]	Rp$_{0.2}$ [MPa]	A [%]	Ag [%]
0.24C-1.60Mn-0.12Si-1.41Al-0.17Mo	1170-1420	1030-1150	4-9	3-5
0.2C-1.63Mn-1.63Si	1280-1510	1050-1200	4-15	4-11
0.20C-1.40Si-1.87Mn	869-997	512-626	16-26.8	13-23

3.1.2 **Process Design**

It is possible to determine the heat treatment parameters of the Q&P treatment to obtain distinct phase fractions and compositions of retained austenite with theoretical models. The fraction of martensite and austenite at quenching temperatures below Ms can be calculated through the Koistinen - Marburger relationship (Equ. 5) [8].

$$f_m = 1 - e^{-1.1x10-2(M_S - QT)}$$ (Equ. 5),

where the fraction of austenite, which transforms to martensite during quenching to a quenching temperature QT, is represented by f_m.

Besides the calculation of fractions of martensite, a graphical model for Q&P process design exists. The maximum fraction of retained austenite can be determined, whereby partitioning kinetics as well as carbide precipitation are neglected and all carbon is partitioned into austenite [8].
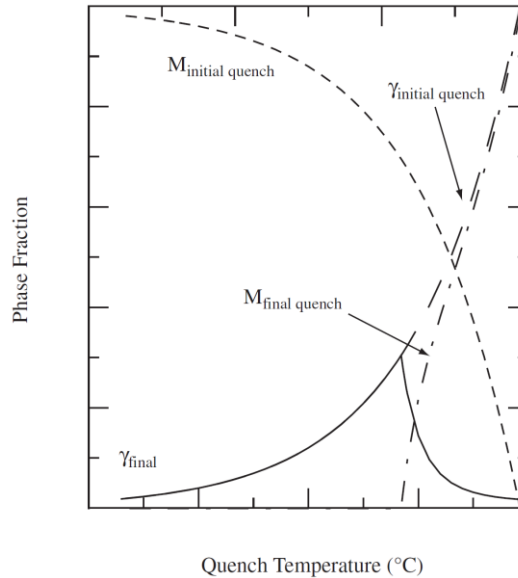

Fig. 15: Predicted microstructure after Q&P treatment. The quench temperature QT determines the phase fraction which can be obtained [8].

Fig. 15 shows a shematic diagram of the microstructure evolution during Q&P treatments. The initial fraction of martensite and austenite after quenching to QT is given by the dashed lines ($M_{initial\ quench}$, $\gamma_{initial\ quench}$). Based on that, the quench temperature QT below the M_s determines the maximal phase fraction of retained austenite. Lower quenching temperatures lead to smaller austenite fractions, whereas at higher quenching temperatures higher fractions are present. The solid line represents the austenite fraction after partitioning (all carbon is in austenite) at room temperature (γ_{final}). The austenite phase fraction before and after partitioning is equal in the lower temperature regime. In that temperature region, the austenite is highly stabilized by carbon. At the temperature where the solid line shows a peak, the maximum phase fraction of retained austenite that can be stabilized with carbon is reached. Above this temperature the fraction of austenite is retrogressive, as the carbon content of the alloy is too low for stabilizing a higher fraction of austenite. Thus, the austenite can´t be stabilized at final quench and new martensite is built during cooling after partitioning [8].

The degree of stabilization, i.e. the amount of carbon in austenite after finished partitioning, can be determined by a thermodynamically - based concept. Constrained carbon equilibrium (CCE) or constrained paraequilibrium (CPE) assumes metastable martensite/austenite equilibrium in the case of constrained or stationary interfaces, which depends on two

conditions, a thermodynamic condition and a unique matter balance [8, 3, 49]. Both terms are presumed equally in this thesis. A detailed discussion about the terminology of CCE and CPE is referenced by Hillert and Ågren [53].

The thermodynamic assumption states equal chemical potentials of carbon in each phase and is fulfilled with an infinite quantity of phase compositions. In this case, the CPE may be represented by the resulting Equ. 6 of Lobo and Geiger [8]:

$$\chi_C^\gamma = \chi_C^\alpha * e^{\frac{76.789 - 43.8T - (169.105 - 120.4T)*\chi_C^\gamma}{RT}} \qquad\qquad \text{(Equ. 6)}$$

χ_C^γ and χ_C^α are the mole fractions of carbon in austenite and ferrite. This concept does not take the influence of alloying elements on carbon activity into account. Therefore, carbon partitioning is completed when the chemical potential in both phases is equal.
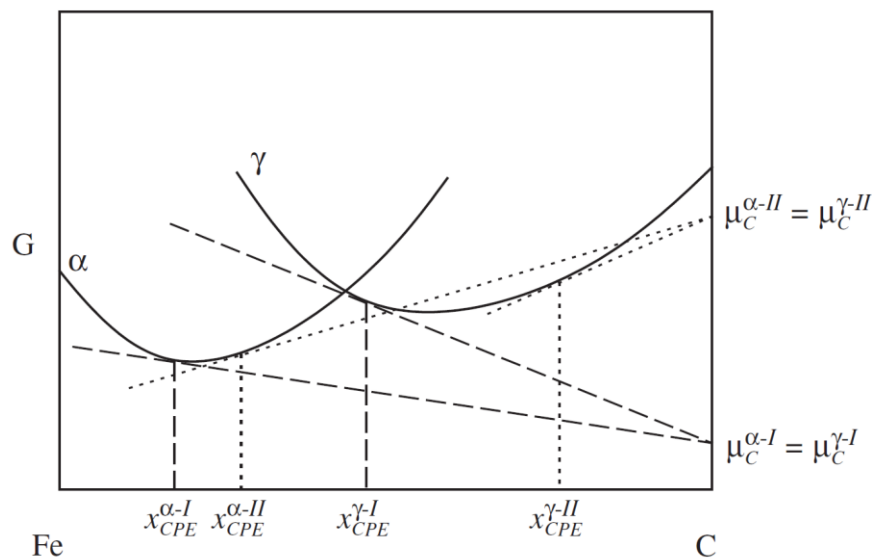

Fig. 16: Two possible CPE conditions (I and II) for the Fe-C binary system in dependency of the molar free Gibb´s energy and carbon content **[8]**.

Fig. 16 demonstrates the tangents of the free energy potentials of ferrite and austenite, which intersect the carbon axis in a single point for carbon equilibrium at CPE. Two of an infinite set of phase compositions for CPE are depicted. The phase composition with $\chi_{CPE}^{\alpha-II}$ and $\chi_{CPE}^{\gamma-II}$ has a higher carbon content and the phase composition with $\chi_{CPE}^{\alpha-I}$ and $\chi_{CPE}^{\gamma-I}$ has a lower carbon content. The actual CPE must satisfy the unique matter balance, which determines the feasible phase composition. It is associated with the stationary martensite/austenite interface and accordingly conserved Fe and substitutional atoms. This

leads to a redistribution of carbon and other interstitials during partitioning. The matter balance is represented by Equ. 7 [8]:

$$f_{CPE}^{\gamma} * \left(1 - \chi_{C_{CPE}}^{\gamma}\right) = f_i^{\gamma} * \left(1 - \chi_c^{alloy}\right)$$ (Equ. 7)

f_{CPE}^{γ} describes the amount of austenite and $\chi_{C_{CPE}}^{\gamma}$ the carbon concentration in austenite at CPE, if partitioning is finished. f_i^{γ} expresses the mole fraction of austenite before partitioning, where χ_c^{alloy} represents the entire carbon content of the steel.

The mass balance is mathematically represented by Equ. 8 and the relationship between the phase fraction of austenite and ferrite is represented by Equ. 9 [8].

$$f_{CPE}^{\alpha} * \chi_{C_{CPE}}^{\alpha} + f_{CPE}^{\gamma} * \chi_{C_{CPE}}^{\gamma} = \chi_c^{alloy}$$ (Equ. 8)

$$f_{CPE}^{\alpha} + f_{CPE}^{\gamma} = 1$$ (Equ. 9)

CPE is achieved when all four equations mentioned above are fulfilled.

Deviation of this calculated retained austenite maxima might be explained by bainite formation and incomplete carbon partitioning. Similarly, cementite formation due to higher partitioning temperatures and longer time leads to an instability of austenite [44].

3.2 Bainitic Steels

Bainitic steels are characterized by a significant amount of bainitie, which can be obtained by appropriate selections of thermal treatment parameters. Furthermore, bainitic steels with a combination of high ductility and strength have in common that cementite formation at the interfaces is suppressed by the addition of Si. As a result, instead of brittle cementite ductile austenite is present.
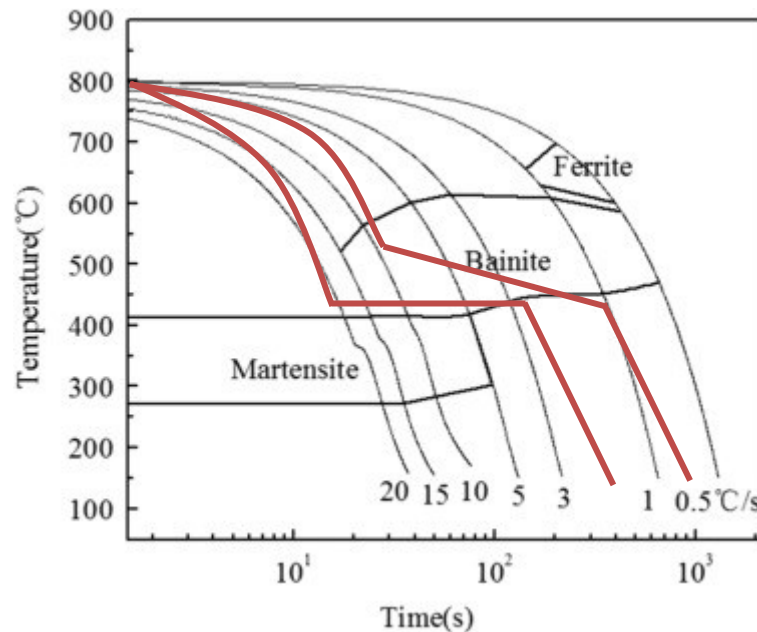

Fig. 17: Common thermal treatments for bainitic steels plotted in a CCT-diagram **[54]**

Fig. 17 shows thermal treatments for bainitic steels plotted in a continuous cooling transformation (CCT) diagram. Common treatments are isothermal holding at a defined quenching temperature or quenching with continuous cooling in the bainite region (marked with red) [55]. Furthermore, continuous cooling from annealing temperature, quenching in multiple steps and thermomechanical processes are possibilities to obtain bainite [56, 57].

As soon as bainite forms during processing, carbon diffuses into the surrounding austenite, thereby stabilizing the untransformed austenite [23]. Depending on alloying concept also other phases, e.g. ferrite or martensite may occur. For further information about austenite stability and influence of alloying elements on phase formation see chapter 2.1 and chapter 4.

Chemical composition and mechanical properties achievable with bainitic microstructures in literature are listed in Table 3 [23, 55].

Table 3: Mechanical properties achievable with bainitic microstructure

Composition	Rm [MPa]	Rp$_{0.2}$	A [%]	γ$_{ret}$ [%]
0.22C-1.83Si-2.02Mn-0.23Mo	986 ± 13	620 ± 15	18.5 ± 0.3	4.0 ± 0.2
0.22C-1.79Si-21.98Mn-1.00Cr-0.23Mo	1185 ± 26	786 ± 20	11.7 ± 0.9	4.8 ± 0.3
0.29C-1.50Si-2.25Mn-0.26Mo	1796 ± 21	1240 ± 31	18 ± 1	3 ± 1
0.21C-1.46Si-1.56Mn-1.49Cr-0.24Mo	1306 ± 16	999 ± 54	25 ± 3	12 ± 1

The ductility of bainitic steels is controlled by the volume fraction of retained austenite. Austenite transforms under an applied load into martensite via the TRIP effect, which enhances the ductility. Plastic deformation is a mechanism based on dislocation movement. The strength of bainitic steels is a result of the obstruction of dislocation motion by a variety of obstacles (fine films of retained austenite, grain boundaries, solute atoms, etc). As plastic deformation at first focuses on softer phases, blocks of retained austenite should be avoided and fine austenite films are preferable. Toughness is effectively enhanced by a reduction of the effective grain size and the absence of hard brittle phases, e.g. high C martensite and cementite. [23].

4 Influence of Alloying Elements

This chapter gives an overview of chemical elements and their influence on microstructure and thermal treatments, especially dealing with those elements important for the materials analyzed in this thesis.
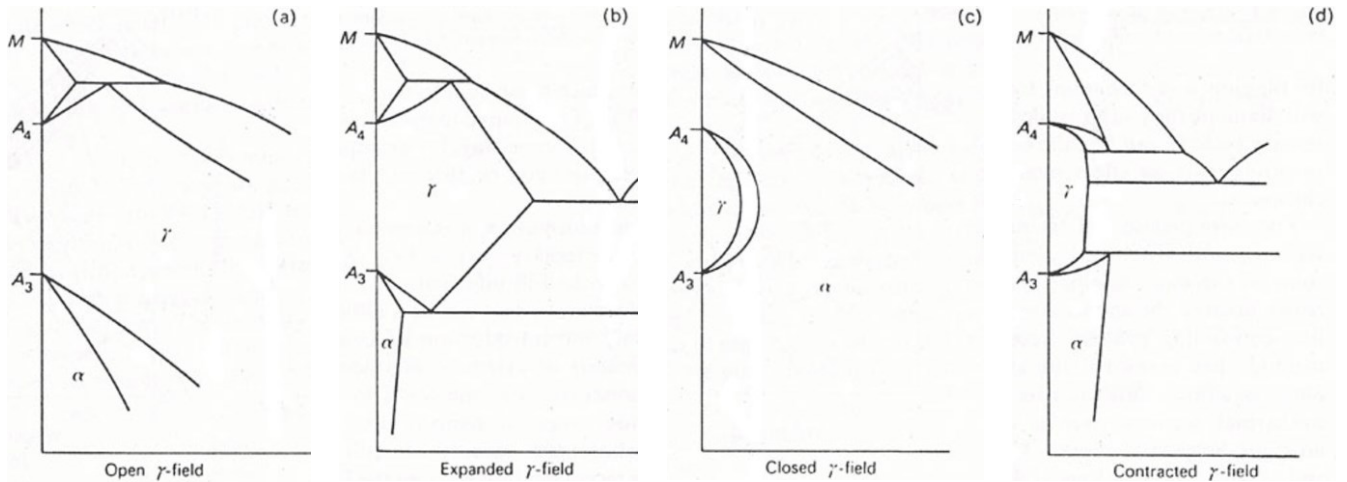

Fig. 18: Influence of alloying on the Fe-C equilibrium diagram.
(a) Ni, Co, Mn (b) C, N (c) Al, Si, P (d) Cr, Ti, Ta, Mo, V **[58]**.

Alloying elements have a direct influence on the iron - carbon equilibrium diagram as demonstrated by Fig. 18. Elements such as nickel (Ni), cobalt (Co) and manganese (Mn) open the austenite field and depress the phase transformation of austenite to lower temperatures (Fig. 18 a). Carbon (C) and nitrogen (N) expand the austenite field over wider compositional limits (Fig. 18 b). Whereas, aluminium (Al), silicon (Si) and phosphorus (P) restrict the formation of γ (Fig. 18 c). Chromium (Cr), titanium (Ti), tantalum (Ta), molybdenum (Mo), vanadium (V) enlarge the ferrite field and contract the austenite section (Fig. 18 d) [3, 58].

In addition, the transformation diagrams are affected by alloying elements, e. g. Mo, Cr, Ni, Mn shift the entire TTT to later times [59].
Mn, Cr, Mo and Ni reduce the temperature window for bainite and delay the incubation time for ferrite and bainite, which leads to increased amounts of austenite at quenching temperature [49].
The formation of carbides reduces the amount of carbon for partitioning. According to this, the carbides act as carbon sinks. Transition carbides reduce the potential of carbon enrichment in austenite. Cr, Mo, V are strong carbide forming elements. A formation of Cr, Mo, V carbides partially withdraws the carbon from the austenite [3].

Si, Al, P are insoluble in cementite and impede its formation. This is due to a required diffusion of the elements away from the growing cementite grain [3, 44]. Thus, the transition from early-stage tempering (where ε or η carbides are present) to later-stage tempering (where θ-Fe3C is present) is delayed by Si [8]. Partial replacement of Si with Al or P improves the hot dip coatability and Al leads to a lower fraction of retained austenite as it is a strong ferrite stabilizer [44]. Higher content of Si causes higher yield strength values [3].

5 Materials and Methods

5.1 Investigated Materials

In this thesis, two different steels have been chosen and investigated regarding microstructural and mechanical properties. The materials differ mainly in carbon content, to gain information about the influence of heat treatment and partitioning of carbon on stabilization of retained austenite. Furthermore, the effect of different content of silicon, manganese, chromium and molybdenum on materials behavior is of interest. The exact chemical compositions of the specimen materials are given by Table 4.

Table 4: Actual chemical compositions of the investigated materials.

	Elements in Weight percent [wt%]					
	C	Si	Mn	Cr	Mo	V
AFP	0.28	0.58	1.43	0.13	0.01	0.10
SBain	0.40	1.08	0.84	1.10	0.71	0.10

The **first alloy** is a 30MnVS6 steel. The specimen material is a cold forged wire and has been delivered in a coil with 20 m in length and 11 mm in diameter.

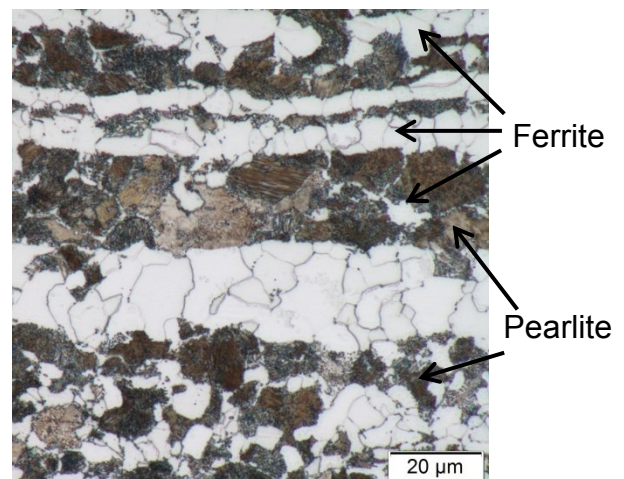Fig. 19: Delivery condition of the 30MnVS6 steel.

Fig. 20: Pearlitic, ferritic microstructure of the delivery condition of the 30MnVS6.

Fig. 19 shows the delivery condition. The microstructure has been observed by optical microscopy and is ferritic, pearlitic as shown in Fig. 20.

The delivered material has a tensile strength of Rm = 782 MPa, an elongation at fracture of A = 24.3% and a hardness of 223HV10.

The 30MnVS6 steel is a micro alloyed AFP (German: "Ausscheidungshärtender" = precipitation hardening, ferritic, perlitic steel) steel. AFP steels are characterized by ferritic perlitic matrix and a precipitation of fine carbides (VC) during controlled cooling from austenitization. As a result, a tempering treatment is not necessary and costs can be reduced [60].

The wire was straightened and was exposed a subsequent stress relieving treatment as shown in Table 5 to resolve residual stresses. The treatment causes no change in microstructure, i.e. the delivery state is the initial state for further processing.

Table 5: Process parameter for stress relieving

Diameter [mm]	Temperature [°C]	Heating Rate [K/min]	Holding at Temperature [min]	Furnace cooling [K/s]
11	650	5	20	2.5

The **second alloy** has a higher content of carbon, silicon, chromium and molybdenum. For simplification, the specimen material will be designated as SBain in this thesis. The SBain specimens were delivered in blocky shape.
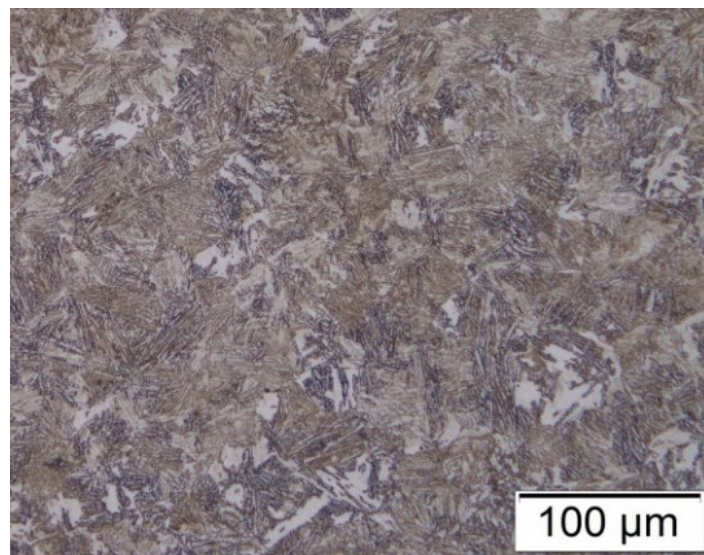

Fig. 21: Bainitic microstructure of the SBain.

The microstructure was observed by optical microscopy and is bainitic as shown in Fig. 21. The fraction of retained austenite was determined with 23.7% by means of XRD and the hardness according to Vickers is 396 HV 10.

5.2 Setup of Experiments and Thermomechanical Calculations

<u>Light microscopy</u>

The investigation of microstructure was carried out by optical microscopy and etching with Nital (HNO_3) as well as colour etching according to Klemm. Nital (an ethanol nitric acid) is more corrosive, the higher the carbon content is, consequently the higher the carbon content the darker the appearance of the phase, e.g. ferrite is blocky and white with no substructure. Klemm´s reagent (a sodium thiosulfate solution potassium metabisulphite) produces a surface layer. The thickness of the layer depends on carbon content and etching time. In this thesis, martensite and bainite may appear blue or brown depending on carbon content and grain angle, while ferrite is blue or violet with no substructure. Austenite, carbides, phosphides etc. will remain either white or in their own colour. Hence, regions with higher alloying content than the neighboring areas will appear brighter [61, 62]. The microstructure was analyzed with Olympus® Stream (Stream Motion Desktop) in combination with data received from the dilatometer to obtain phase fractions.

<u>Dilatometry</u>

Dilatometry provides an opportunity for controlled quenching and reheating to defined temperatures for small specimens. Hence, the dilatometer DIL 805 L/A from TA Instruments was used to gain information about transformation kinetics and heat treatments in this thesis. Transformation temperatures were determined by the tangent method using the length change data from the dilatometer. The tangent method provides a possibility to obtain the start and finish temperature of phase transformation during cooling. Thus, the transformation temperatures were evaluated by Origin® with a magnification of 200 %.
To confirm that a transformation at a certain temperature appears, the derivation of length by time was formed and illustrated as a function of temperature.
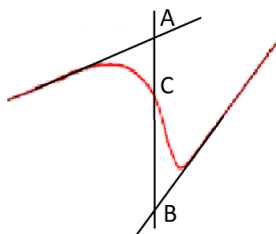

$$f_{\alpha'} = \frac{BC}{AB} \qquad \text{(Equ. 10)}$$

$f_{\alpha'}$…fraction of martensite

AB, BC…sections according to Fig. 22

Fig. 22: Lever rule applied for martensitic transformation.

The lever rule was applied on the length change versus temperature curves from dilatometer data as shown in Fig. 22 to evaluate degree of austenite to martensite transformation at distinct temperatures. The formed fraction of martensite was calculated with Equ. 10. The calculation assumes complete austenite to martensite transformation. Thus, a fraction of retained austenite determined by XRD after finished transformation at RT was deducted from the calculated fraction of martensite and added to the calculated fraction of austenite.

The samples for experiments in the dilatometer are 10.2 mm in length and 4 mm in diameter.

d0	L0	d1	h	Lc	Lt
4±0,060	20	M6	15	24	62
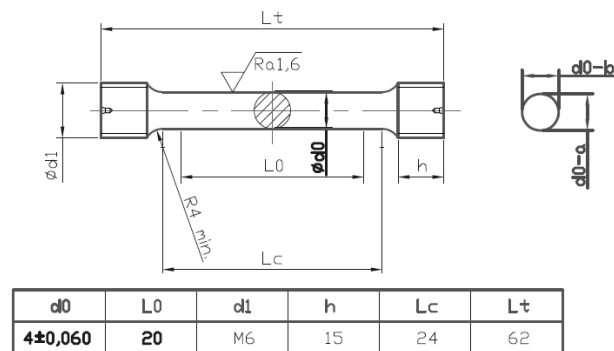
Fig. 23: Sketch of tensile specimen.

Tensile tests

Heat treatment of tensile test specimens was performed in the dilatometer. All tensile specimens were machined in rolling direction according to Fig. 23 (DIN 50125:2003-05 [63] standards) with a gage length L0 of 20 mm and a diameter d0 of 4 mm. Tensile testing was performed with the Z250 – universal testing machine from Fa. Zwick at room temperature and a force transducer with 250 kN according to DIN EN 6892-1, A224 [64] standards.
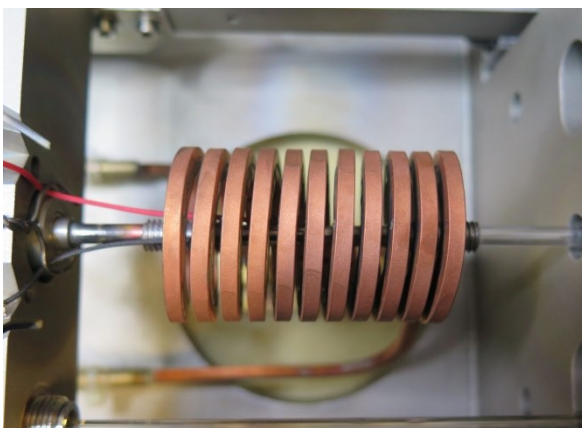

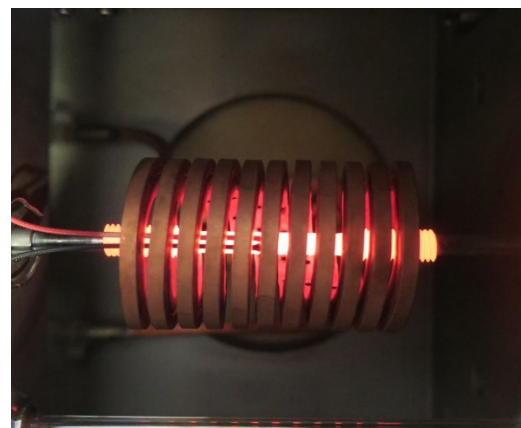Fig. 24: Setup for heat treatments of tensile specimens before processing.

Fig. 25: Setup for heat treatments of tensile specimens during processing.

Fig. 24 and Fig. 25 show the setup for heat treatment of tensile specimens before and during processing, showing that the gage length is within the coil. Owing to the dimensions of the tensile specimens (Fig. 23), an induction - coil of 5 cm in length was chosen.

Harndess measurement

The hardness according to Vickers was measured with Q-ness Q10A+. Therefore, 5 indents at different positions were made and the average hardness was calculated in accordance with the ÖNORM EN ISO 6507-1 [65] standards.

X-ray diffraction measurements

To receive fractions of retained austenite the specimens were investigated with X-Ray diffraction (XRD). Therefore, the D8 Discover diffractometer from Brucker AXS operating with Mo-Kα (wavelength = 0.7107 Å) was used. Calculations of retained austenite were done with "Direct Comparison" method in consideration of frequency values (values of R - according to ASTM E975-08 [66] standards).

Setup of simulations

The appearing phases in equilibrium of selected chemistry were investigated with Thermo-Calc® (product version: 5.0.06053) using the TCFE8 database.

Transformation kinetics at different cooling rates were calculated with JMatPro® (product version: 8.04). The software enables a demonstration of phase transformation diagrams.

The diffusion constant D_0 was calculated by MatCalc version 6 and fe-2.059.tdb and mc_fe.ddb.

6 Results and Discussion

Heat treatment parameters for Q&P and bainitic heat treatments are strongly dependent on transformation temperatures such as Ms, Bs in dependence of cooling rate. Thus, the chapter "Results and Discussion" is divided in four sections. The chapter "Determination of Transformation Behavior during Cooling" concentrates on the determination of transformation behavior for a selection of suitable Q&P and bainitic heat treatments. The chapter "Q&P and Bainitic Heat Treatments" use these results to determine the specimen's behavior during processing. Whereas, in chapter "Comparison of Mechanical Values" the mechanical properties of selected treatments are evaluated. Subsequently, the experimentally determined properties are analyzed in chapter "Discussion of Q&P and Bainitic Heat Treatments and their Mechanical Behavior".

6.1 Determination of Transformation Behavior during Cooling

6.1.1 Calculations of Transformation Behavior and Phase Stability and Evaluation of Heat Treatment Parameters

The evaluation of heat treatment parameters for the determination of the transformation behavior during cooling was carried out by the aid of Thermo-Calc and JMATPro calculations. Thermodynamic calculations with Thermo-Calc were used to evaluate the Ac3 temperature.
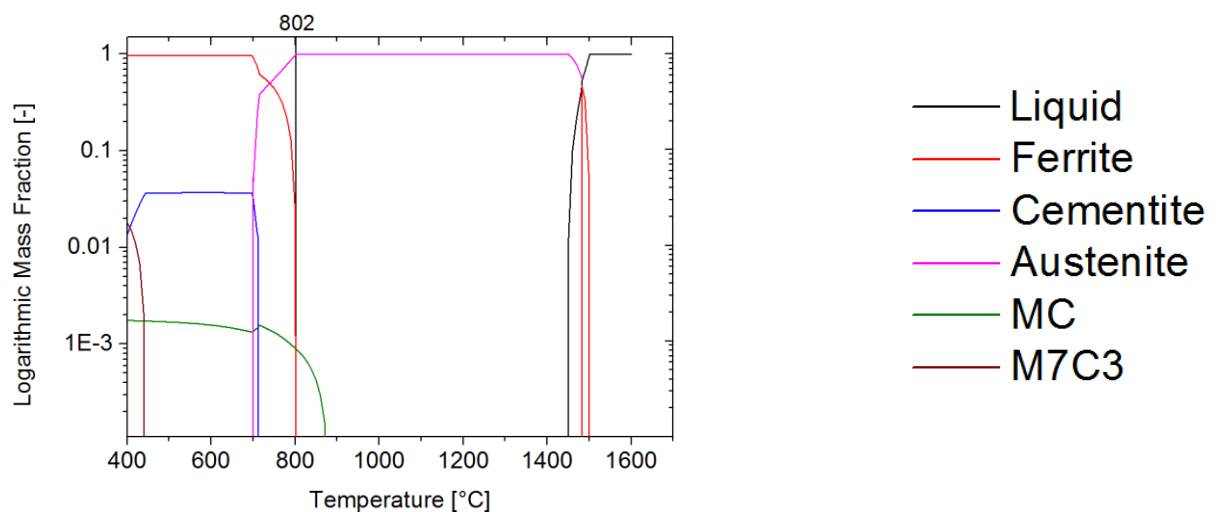

Fig. 26: Phases in equilibrium in dependency of temperature of the AFP steel obtained with Thermo-Calc (TCFE8 database).

The mass fraction of the phase as function of the temperature are illustrated in Fig. 26 for the AFP steel. The mass fraction is shown in logarithmic scale to illustrate the appearance of carbides, which are only present in small fractions. Cementite formation occurs at temperatures lower than 720°C. MC carbides are stable up to 870°C and M7C3 carbides dissolve at 450°C. The Ac_3 temperature is at 802°C.
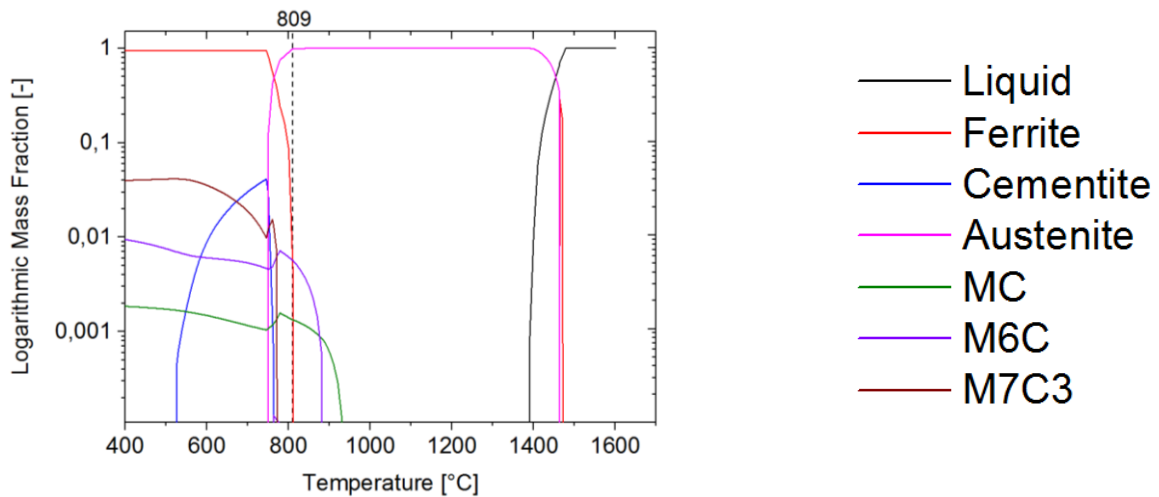

Fig. 27: Phases in equilibrium in dependency of temperature of the SBain obtained with Thermo-Calc (TCFE8 database).

Fig. 27 shows the phases as function of the temperature for the SBain in dependence weight percent and temperature. The Ac_3 temperature is at 809°C. MC carbides are present up to temperatures of 930°C. M6C carbides are stable at temperatures lower than 880°C. M7C3 and cementite are dissolved at temperature higher than 770°C.
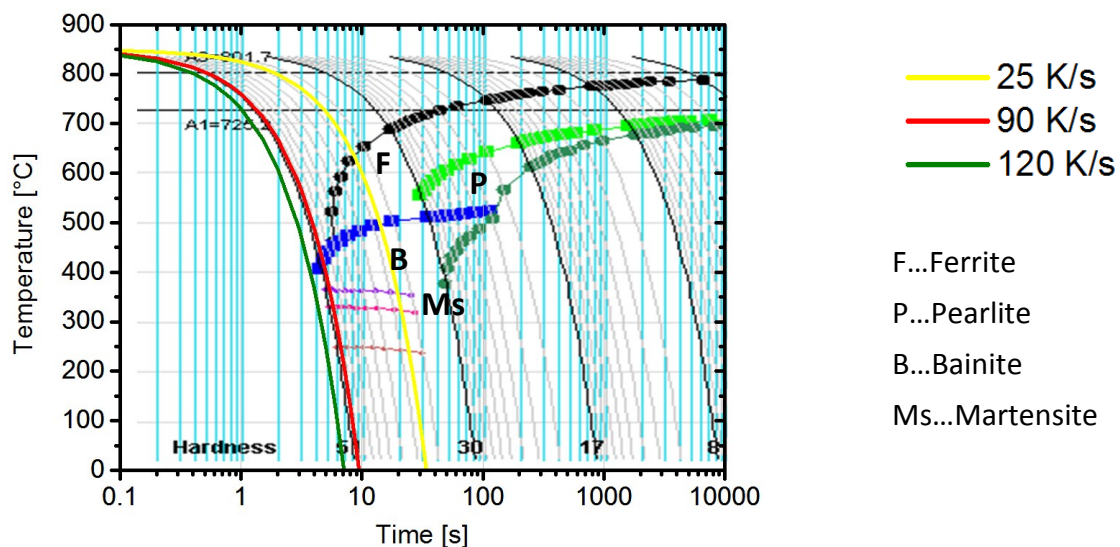

Fig. 28: CCT diagram of the AFP steel calculated with JMatPro®. The yellow, red and green line represent the cooling curve for 25 K/s, 90 K/s and 120 K/s respectively. A grain size of 20 μm and an austenitization temperature of 850°C were used for calculations.

The CCT diagram of the AFP steel is shown in Fig. 28. The areas of possible phases are indicated by F; P; B; Ms, where F denotes the ferritic, P the pearlitic, B the bainitic phase and Ms the martensite start temperature. The dark green line limits the pearlite and bainite region and indicates finished phase formation. It is evident that transformation occurs rapid and the transformation ranges of the phases are close to each other. According to the CCT, a cooling rate of 120 K/s, this is represented by the green line, results in a pure martensitic microstructure. The martensitic microstructure exhibits fractions of bainite at cooling with 90 K/s, as indicated by the red line. The yellow line demonstrates a cooling rate of 25 K/s, which leads to a ferritic, bainitic, martensitic microstructure with little fractions of pearlite. The Ms temperature is around 350°C marked with violet. According to the summery of Gorni as mentioned in chapter 2.3 Iron - Carbon Martensite Equ. 4, the martensite start temperature for the AFP steel is Ms = 371°C.
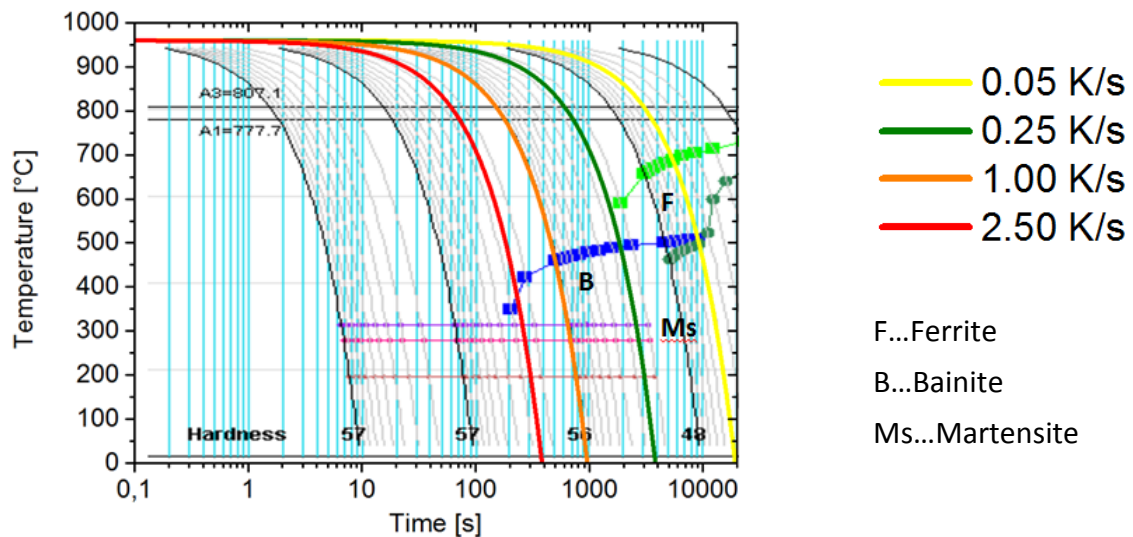

Fig. 29: CCT diagram of the SBain calculated with JMatPro®. The yellow, green, orange and red lines represent the cooling curves for 0.05 K/s, 0.25 K/s, 1 K/s and 2.5 K/s respectively. A grain size of 50 µm and an austenitization temperature of 960°C were used for calculations.

Fig. 29 shows the CCT diagram of the SBain steel. A key difference compared to the AFP steel is that the transformation is delayed to longer times. Cooling with 2.5 K/s, results in a martensitic microstructure with at least some fractions of bainite, whereas a cooling rate of 1 K/s and 0.25K/s generates a bainitic, martensitic microstructure. According to the CCT, cooling to room temperature with 0.05 K/s causes a mostly ferritic microstructure with small amounts of bainite. According to the CCT martensite start temperature is around 310°C. The calculated Ms temperature with Equ. 4 of chapter 2.3 Iron – Carbon Martensite is Ms = 306°C for the SBain.

In view of the calculations with JMatPro to receive conditions consisting of martensite, martensite + bainite and martensite + bainite + ferrite, different cooling rates were chosen for the AFP steel to determine the transformation kinetics by experiments. An austenitization temperature of 850°C was chosen as Ac3 was evaluated at 802°C. The parameters for the experiments on the cooling behavior are listed in Table 6. Quenching with 120 K/s was chosen to determine pure martensitic transformation. While cooling rates of 90 K/s and 25 K/s should lead to a bainitic phase transformation. The annealing temperature, the heating rate, the holding time at austenitization temperature and the quenching rate are indicated by T_A, $\dot{t}_{heat}$, t_A, QR, respectively.

Table 6: Experimental parameters for different cooling rates chosen for the AFP steel. The heating rate, the annealing temperature, the holding time at austenitization temperature and the quenching rate are indicated by $\dot{t}_{heat}$, T_A, t_A, QR, respectively.

$\dot{t}_{heat}$ [K/s]	T_A [°C]	t_A [min]	QR to RT [K/s]
2.5	850	30	120
2.5	850	30	90
2.5	850	30	25

The cooling rates and austenitization temperatures for the SBain are illustrated in Table 7. The austenitization temperature was set to 960°C because carbides are present in equilibrium up to 870°C. Cooling rates were determined according the calculations with JMatPro. A cooling rate with 2.5 K/s was chosen to achieve pure martensite and cooling with 1 K/s should lead to a mixture of bainite and martensite.
To identify the occurrence of ferrite, cooling rates of 0.25 K/s and 0.05 K/s were chosen.

Table 7: Experimental parameters for different cooling rates of the SBain. The heating rate, the annealing temperature, the holding time at austenitization temperature and the quenching rate are indicated by $\dot{t}_{heat}$, T_A, t_A, QR, respectively.

$\dot{t}_{heat}$ [K/s]	T_A [°C]	t_A [min]	QR to RT [K/s]
2	960	30	2.5
2	960	30	1
2	960	30	0.25
2	960	30	0.05

6.1.2 **Cooling Behavior of the AFP steel**

Received data from the dilatometer and the documentation of the microstructure offer an opportunity to give a statement about appearing phases.
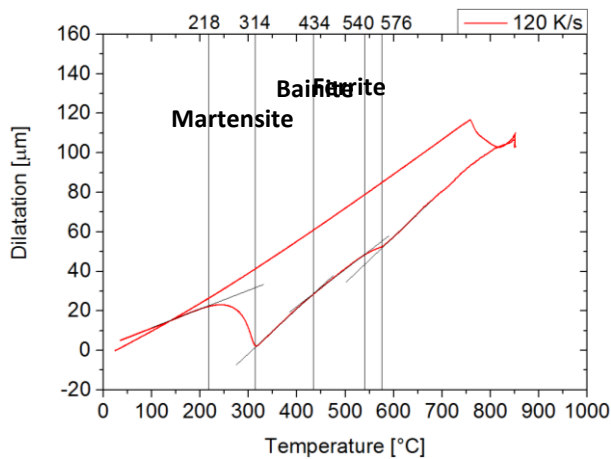

Fig. 30: Dilatation in dependence of temperature of the specimen quenched with 120 K/s. The vertical lines restrict the areas of phase formation.
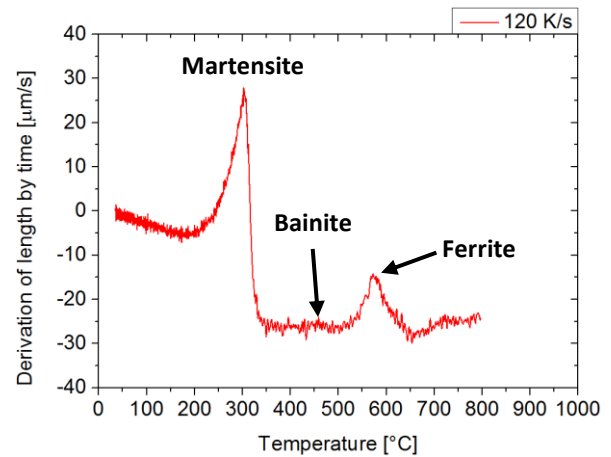

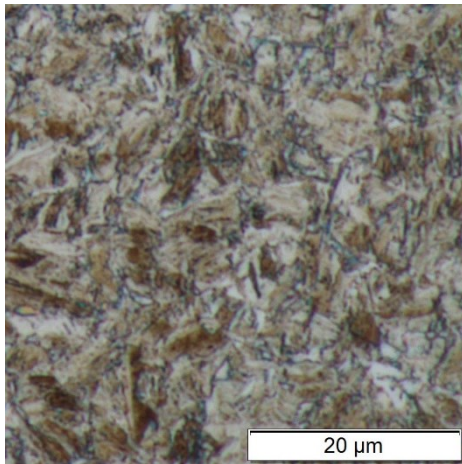Fig. 31: Derivation of the cooling curve for the specimen quenched with 120 K/s.

Fig. 32: Microstructure of the specimen quenched with 120 K/s and etched with Nital.
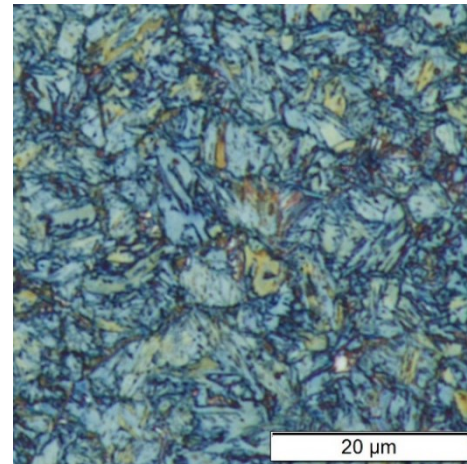

Fig. 33: Microstructure of the specimen quenched with 120 K/s and colour etched according to Klemm.

Fig. 30 illustrates the volume change through the measured length change (dilatation) of the specimen during heating and cooling in dependence of temperature. During heating, austenite formation results between 750°C and 820°C as visible by the contraction of the length. During cooling two effects cause an increase (or lower reduction) of length. As the transformation of fcc to bcc leads to an increase of length, these reactions were ascribed to bainite, ferrite and martensite formation. By using the tangent method, the ferrite formation was assumed between 576°C and 540°C and the bainite formation between 540°C and 434°C. The ferrite finish and the bainite start temperature of 540°C is an approximation, as a separation of the formation of both phases was not clearly possible by tangent method. The

Ms temperature was evaluated with 314°C and at temperatures lower than 218°C no further formation of martensite is visible.

The derivation of length with respect to time of the cooling curve is depicted in Fig. 31 as a function of temperature and shows phase transformation indicated by a clearly visible peak. The martensite peak is located between 350°C and 190°C, while ferrite and bainite is demonstrated by peaks between 430°C and 650°C.

The microstructure of the observed specimen analyzed with optical microscopy is illustrated by Fig. 32 and Fig. 33. Displaying the microstructure etched by Nital (see Fig. 32) and phase analyses by Olympus® Stream motion (see chapter 5.2) enables the determination of a fraction of ferrite of 5 %. Ferrite can be distinguished as it is not etched by Nital and appears bright. Fig. 33 depicts the microstructure colure etched according to Klemm. The martensitic phase is blue with a needled shaped structure and the phase analysis provides a fraction of 85 %, while ferrite is bright blue with no structure. Bainite appears as brown with a fraction of 10 % and austenite or carbides are white with no relevant fraction [61].
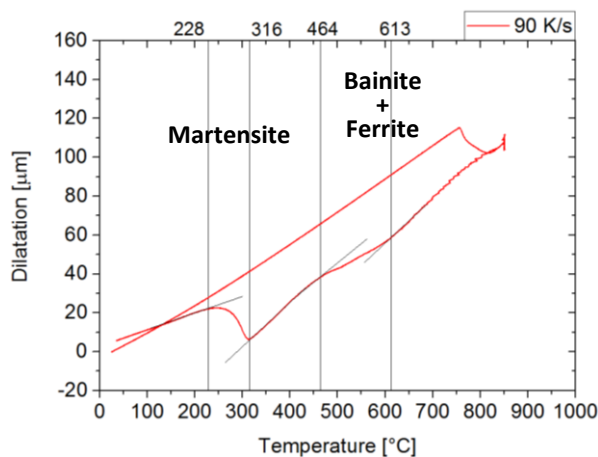

Fig. 34: Dilatation in dependence of temperature of the specimen quenched with 90 K/s. The vertical lines restrict the areas of phase formation.
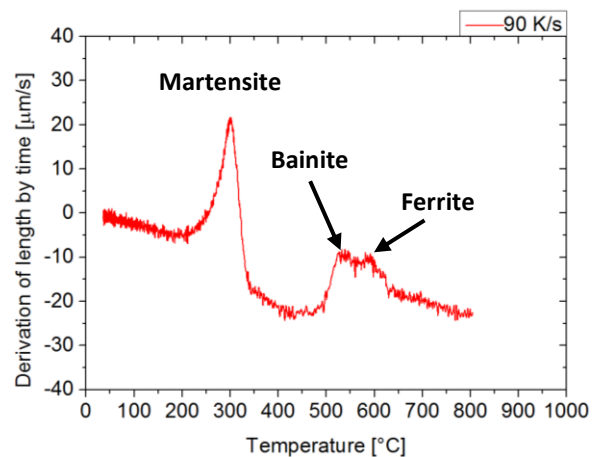

Fig. 35: Derivation of the cooling curve for the specimen quenched with 90 K/s.
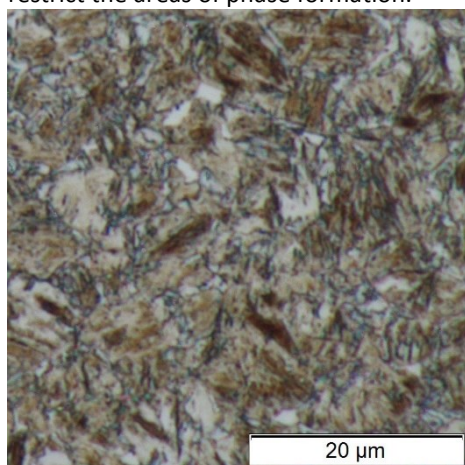

Fig. 36: Microstructure of the specimen quenched with 90 K/s and etched with Nital.
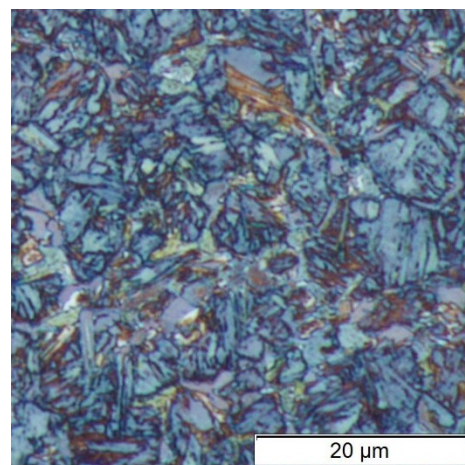

Fig. 37: Microstructure of the specimen quenched with 90 K/s and colour etched according to Klemm.

Fig. 34 illustrates the dilatometer curves of the specimens cooled with 90 K/s in the dilatometer. Between 316°C and 228°C martensitic transformation appears. The length variation between 613°C and 464°C indicates several phase transformations. This is specified by Fig. 35 where two peaks appear between 650°C and 460°C. Fig. 36 and Fig. 37 confirm the assumption of multiple phase transformation, as the microstructure consists of martensite, bainite, ferrite and austenite (or carbides). Hence, a separation of the regions of ferrite and bainite formation by dilatometer data was not possible. The ferrite phase fraction was determined with 7%, the bainitic with 15% and the martensitic with about 78% using the image analysis software Olympus® Stream motion.
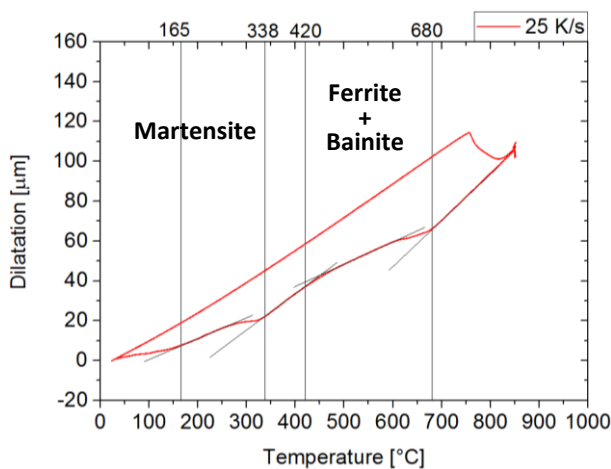

Fig. 38: Dilatation in dependence of temperature of the specimen quenched with 25 K/s. The vertical lines restrict the areas of phase formation.
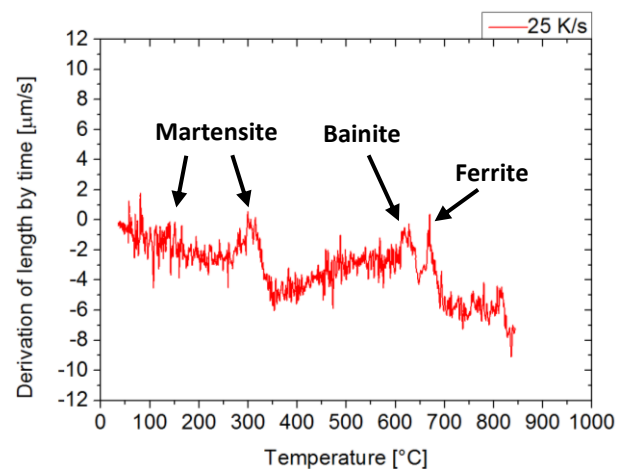

Fig. 39: Derivation of the cooling curve for the specimen quenched with 25 K/s.
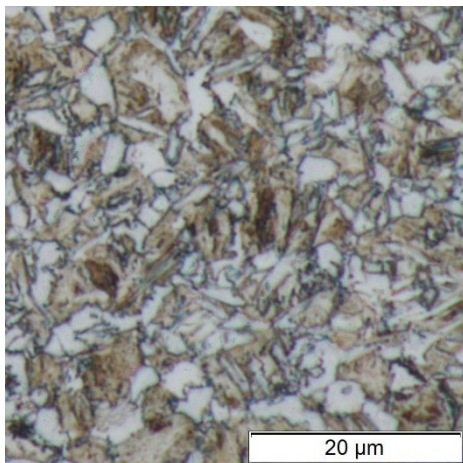

Fig. 40: Microstructure of the specimen quenched with 25 K/s and etched with Nital.
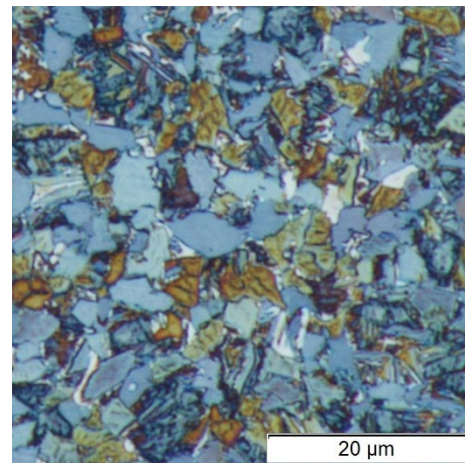

Fig. 41: Microstructure of the specimen quenched with 25 K/s and colour etched according to Klemm.

The region between 680°C and 420°C in Fig. 38 shows that cooling with 25 K/s results in multiple phase transformation. The ferrite formation starts at 680°C, whereas the bainite formation might start at approx. 620°C. It was not possible to clearly separate the ferrite and bainite formation, similar to the cooling rates shown before. The martensite formation starts at 338°C. It is assumed that another martensitic transformation starts at 165°C. The peaks in Fig. 39 approve the formation of several phases. By means of the observation of the microstructure (Fig. 40 and Fig. 41) ferritic, bainitic, martensitic and austenitic phases are determinable. An increase in the fraction of ferrite to 25% was obtained by Fig. 40. The martensite was determined with 49% and the bainite with 25% by Fig. 41. The fraction of retained austenite or carbides was measured with 1% by Olympus® Stream motion.

6.1.3 **Cooling Behavior of the SBain**

The results of investigated cooling rates for the SBain by dilatometer measurements and optical microscopy are listed in this chapter.
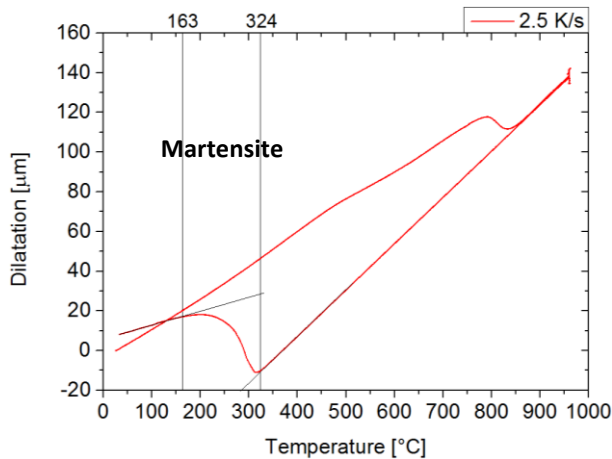

Fig. 42: Dilatation in dependence on temperature of the specimen quenched with 2.5 K/s. The vertical lines restrict the area of phase formation.

Fig. 43: Derivation of the cooling curve for the specimen quenched with 2.5 K/s.

Fig. 44: Microstructure of the specimen quenched with 2.5 K/s and etched with Nital.
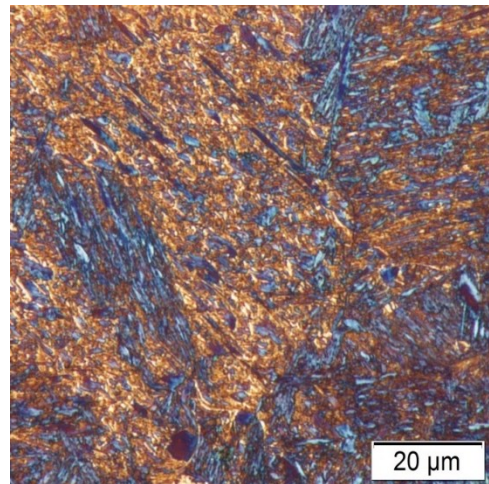
Fig. 45: Microstructure of the specimen quenched with 2.5 K/s and colour etched according to Klemm.

Fig. 42 shows the received data from the dilatometer of the SBain specimen quenched with 2.5 K/s. The length change through the measured length change (dilatation) of the specimen during heating and cooling in dependence of temperature indicates regions of phase transformation. The reduced thermal expansion between 400°C and 600°C of the heating curve might be a consequence of decomposition of retained austenite of the initial state as in this condition 23% retained austenite is present, while the contraction in length between 780°C and 860°C is a result of austenite formation. During cooling, martensite formation appears between 324°C and 163°C. Fig. 43 approves the martensitic transformation. The martensitic microstructure is shown in by Fig. 44 and Fig. 45.

Fig. 46: Dilatation in dependence on temperature of the specimen quenched with 1 K/s. The vertical lines restrict the areas of phase formation.
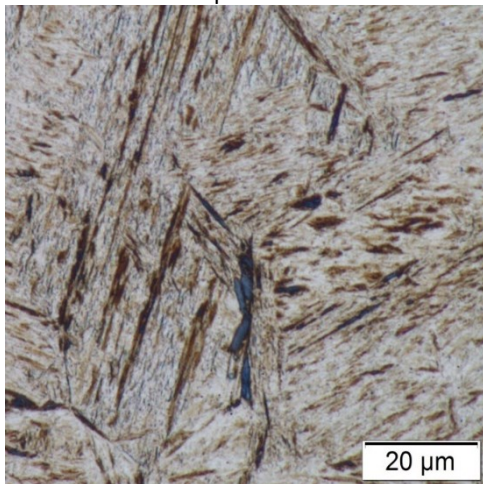

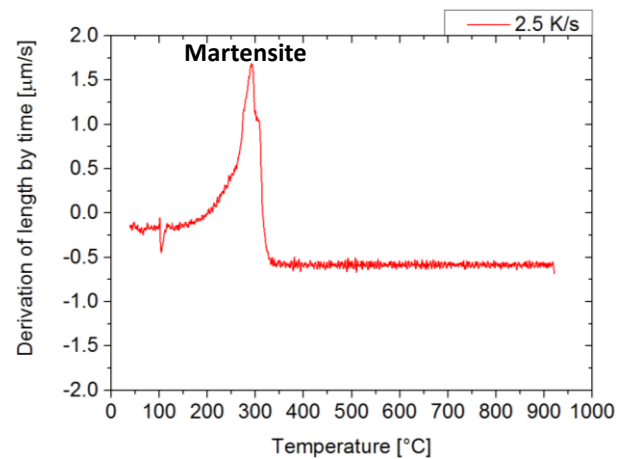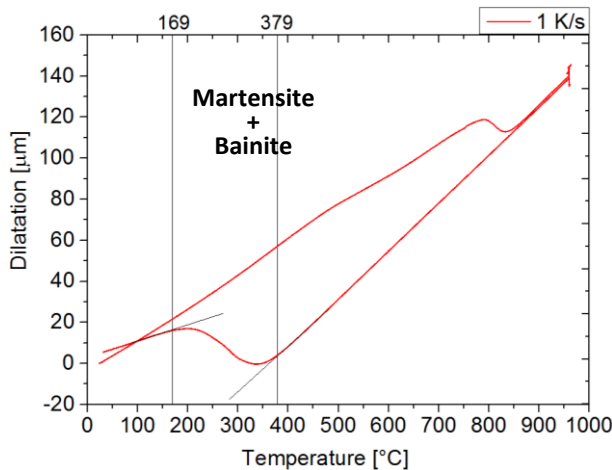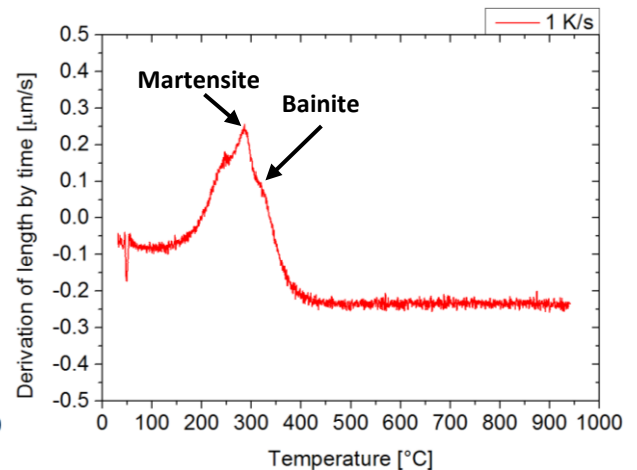
Fig. 47: Derivation of the cooling curve for the specimen quenched with 1 K/s.

Fig. 48: Microstructure of the specimen quenched with 1 K/s and etched with Nital.

Fig. 49: Microstructure of the specimen quenched with 1 K/s and colour etched according to Klemm.

The dilatometer data of cooling with 1 K/s are depicted in Fig. 46 and Fig. 47. No transformation occurs until 379°C. As the martensite start temperature was determined with 324°C upon cooling with 2.5 K/s, several transformations need to be present starting at 379°C. This is approved by a peak between 380°C and 310°C depicted in Fig. 47 which was determined as bainite formation. Austenite to martensite transformation appears at around 320°C and a third peak at 250°C is a second martensite or finished bainite formation, resulting from the segregated initial state of the SBain.

Fig. 48 illustrates a predominately martensitic microstructure. It is assumed that the bright brown regions which are located between the martensite laths and near white areas, that represent austenite, (see Fig. 49) are also martensite or low fractions of bainite.

Fig. 50: Dilatation in dependence on temperature of the specimen quenched with 0.25 K/s. The vertical lines restrict the areas of phase formation.

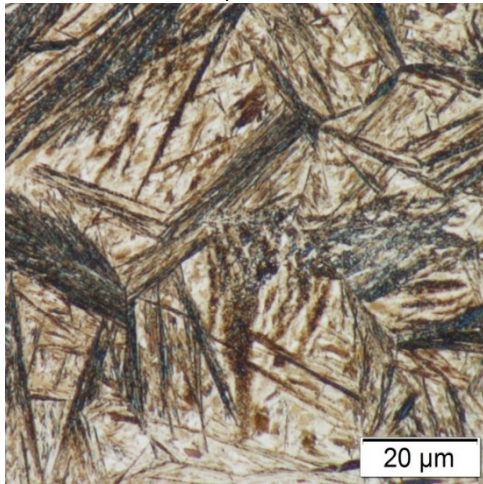Fig. 51: Derivation of the cooling curve for the specimen quenched with 0.25 K/s.

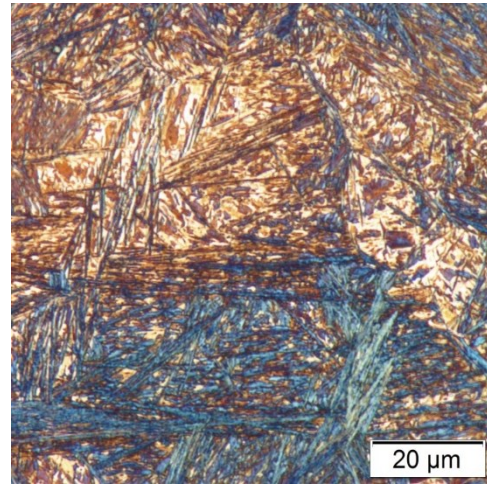Fig. 52: Microstructure of the specimen quenched with 0.25 K/s and etched with Nital.
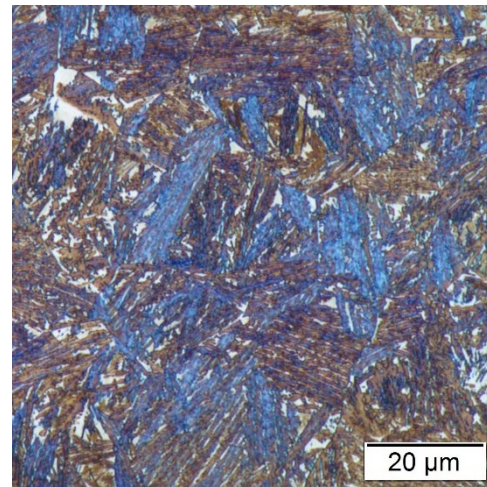
Fig. 53: Microstructure of the specimen quenched with 0.25 K/s and colour etched according to Klemm.

Cooling with 0.25 K/s results in bainitic transformation as indicated by Fig. 50. Bs was determined with 453°C and Bf with 329°C. Fig. 51 approves the incidence of bainitic transformation. The bainitic microstructure is depicted by Fig. 52. According to Fig. 53, a bainite fraction of 93% was determined and the austenite fraction was estimated with 7%.
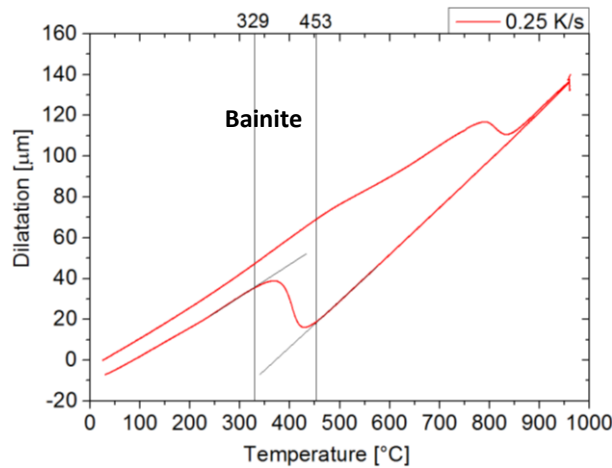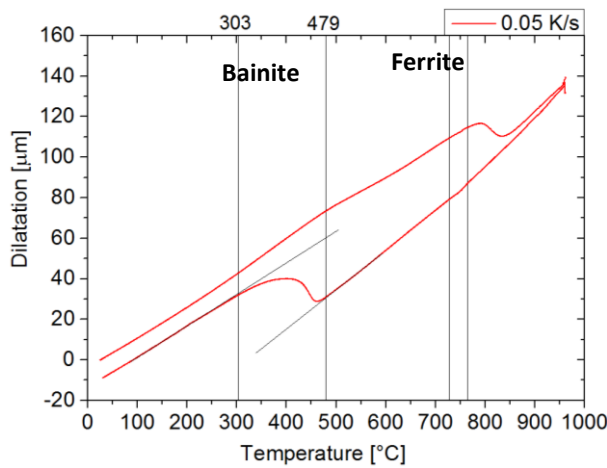
Fig. 54: Dilatation in dependence on temperature of the specimen quenched with 0.05 K/s. The vertical lines restrict the areas of phase formation.
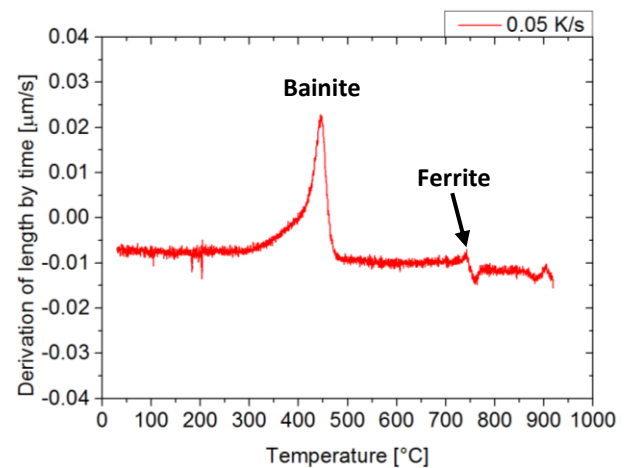
Fig. 55: Derivation of the cooling curve for the specimen quenched with 0.05 K/s.
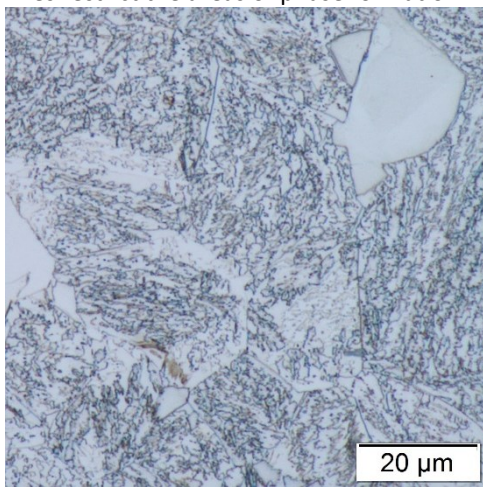
Fig. 56: Microstructure of the specimen quenched with 0.05 K/s and etched with Nital.
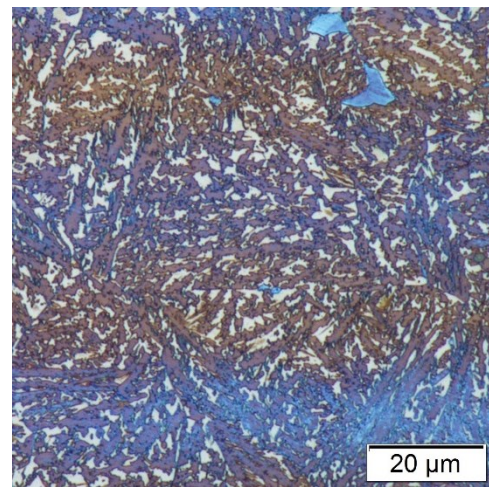
Fig. 57: Microstructure of the specimen quenched with 0.05 K/s and colour etched according to Klemm.

Due to cooling with 0.05 K/s, the Bs of 479°C and Bf of 303°C were determined (see Fig. 54). Between 760°C and 730°C a second phase transformation appears. This transformation is approved by Fig. 55 with the peak at 750°C. This second phase is ferrite as determined by the Fig. 56. It illustrates that the microstructure comprises fractions of ferrite (white) and bainite. The austenite fraction of 14% was determined from Fig. 57.

6.1.4 **Discussion of the Cooling Behavior**

By the analysis of the investigation of different cooling rates information about transformation kinetics of the investigated materials, i.e. the AFP steel and the SBain, is gained. This information about the transformation behavior provides the basis for the selection of the parameters for Q&P and bainitic heat treatments. Especially important are the Ms and Bs temperatures. Therefore, at first the Ms and Bs of the AFP steel are discussed followed by the transformation temperatures of the SBain. Afterwards the simulated data are compared with the experimentally determined data to verify deviations. At last the microstructures are summarized concerning the cooling rates.

Discussion of the Transformation Temperatures of the AFP Steel

Assessing the obtained data from the dilatometer of the AFP steel, it was possible to define martensitic transformation behavior excluding cooling with 25 K/s. The calculated Ms temperature is 371°C (see chapter 6.1.1 and chapter 2.3 Equ. 4), while Ms for cooling with 120 K/s was determined with 314°C and for cooling with 90 K/s with 316°C (see chapter 6.1.2 and chapter 2.3 Equ. 4). The calculated and experimental values do not resemble one another closely. The lower Ms temperatures of cooling with 120 K/s and 90 K/s may be a result of ferrite and bainite formation before martensite transformation appears, where the austenite is enriched with carbon and owing to this the Ms decreases (see chapter 2.3). During cooling of the AFP steel with 25 K/s (Fig. 38) the martensitic formation appears at 338°C and a second change in dilatation appears at 165°C. It was shown in chapter 5.1 that the AFP specimen is strongly segregated. Thus, the change in dilatation at 165°C might be a second martensite formation owing to carbon rich austenitic regions that delay the transformation to lower temperatures. Alternatively, as there is no peak evident in Fig. 39, which show the derivation of length change, this behavior might be a measurement problem of the position sensor.

Regarding the results of bainite formation of the AFP steel (see chapter 6.1.2), it was not possible to find clear evidence of separating the ferrite and bainite formation by applying the tangent method on dilatometer data or by the evaluation of the derivation of length in respect to time. Hence, Bs temperatures of the AFP are an approximation. The determined Bs temperature of 540°C when quenching with 120 K/s corresponds with the calculated value of Bs=542°C (see chapter 2.2, Equ. 3).

Discussion of the Transformation Temperatures of the SBain

In contrast to the AFP steel, start and finish temperatures of phase transformation during different cooling rates of the SBain were easier to determine, as transformation takes place much slower. These results from the higher content of elements (Mo, Cr) which retard the transformation behavior to later times of the SBain (see chapter 5.1 and chapter 4). Ms temperature of 324°C has been determined by cooling with 2.5 K/s, which is comparable with the calculated Ms = 306°C (deviation: -5.6%) of chapter 6.1.1. Cooling with 0.05 K/s (Fig. 54) shows a change in dilatation between 760°C and 730°C. This area was defined as ferritic transformation by observation of the microstructure. The formation of bainite starts, depending on the cooling rate, between 379 and 479°C.

Comparison of the Simulated and Experimentally determined Data
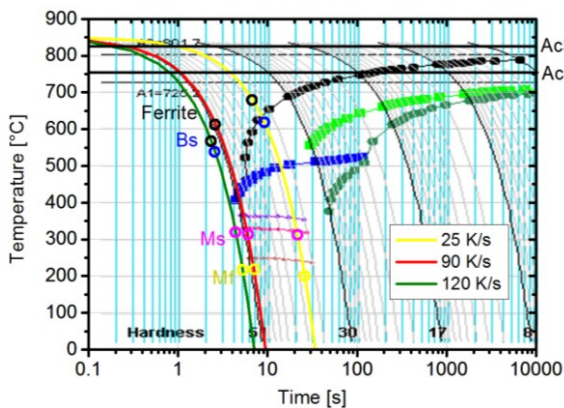
Fig. 58: Experimentally determined tranformation values in comparison with the calculated CCT (JMatPro) for the AFP. The circles represent the experimentally determined start and finish temperature of phase transformation.
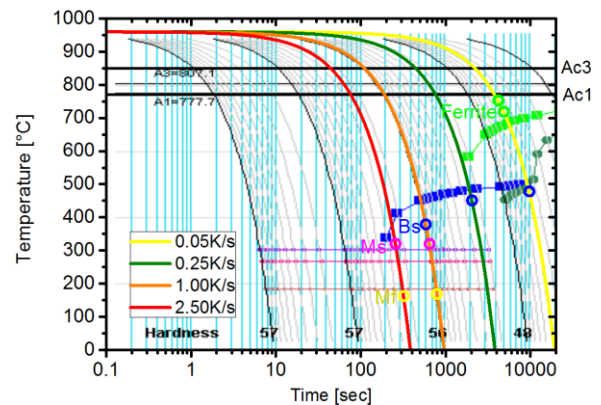
Fig. 59: Experimentally determined tranformation values in comparison with the calculated CCT (JMatPro) for the SBain. The circles represent the experimentally determined start and finish temperature of phase transformation.

Fig. 58 and Fig. 59 compare the experimentally determined and the simulated values of phase transformation during cooling for the AFP steel and the SBain. The experimentally determined Ac_1 and Ac_3 marked by the thick, horizontal, black lines are higher than the by JMatPro calculated Ac_1 and Ac_3 marked by the thin, horizontal, black lines. The different cooling rates were illustrated as a function of temperature and time by the colored lines. Furthermore, the start and finish temperature of every phase transformation are marked. It is important to consider, that the Bs of the AFP steel is an approximation, as a clear separation of ferrite and bainite formation was not possible.

However, the examination of the results of the AFP steel (see Fig. 58) shows that the real transformation behavior of the AFP steel is shifted to shorter times compared to the calculations with JMatPro. Thus, cooling with 120 K/s does not lead to pure martensitic

transformation as originally assumed. It was found that at this cooling rate already ferrite and bainite formation occurs. Consequently, ferrite and bainite formation appears also at cooling with 90 K/s and 25 K/s.

On the contrary, the transformation behavior for the SBain by JMatPro is slightly postponed to longer times, resulting from the higher content of elements (e.g. Mo and Cr) that delay transformation, in comparison to the AFP steel [59]. The calculations (Fig. 59) would suggest that cooling with 2.5 K/s results in martensite and bainite formation. However, dilatometry measurements show only a martensitic transformation for this cooling rate. Furthermore, it was observed by dilatometry that, quenching with 1 K/s leads to martensite and bainite formation, whereas a cooling rate of 0.25 K/s causes pure bainitic transformation. Small amounts of ferrite are only reached by cooling with 0.05 K/s.

Hence, it is evident that the experimental and the calculated data do not fit for both materials. Only the martensite transformation temperatures correspond.

Discussion of Microstructure

Etching with Nital enables a good assessment of the ferrite fraction, as the ferrite clearly distinguishes from the rest of the microstructure. Whereas, etching according to Klemm does not offer the possibility to give a well-funded conclusion about the fractions of retained austenite in this thesis, as white areas in the microstructure might be carbides, retained austenite or untempered martensite [61]. Thus, calculations of fractions of austenite with Olympus® Stream motion are an approximation of actual microstructure.

Table 8 illustrates a summary of the estimated phase fractions achieved with the chosen cooling rates. The abbreviation "udl" indicates under detection limit and describes that the phase fraction is too low to be determinable unambiguously.

Table 8: Phase fractions of the observed cooling rates of the AFP and the SBain. The fractions of ferrite α, bainite α_b, martensite α' and retained austenite γ_{ret} were determined by image analysis.

Steel	Cooling Rate [K/s]	Fraction of α	Fraction of α_b	Fraction of α'	Fraction of γ_{ret}
AFP	120	5 %	10 %	85 %	udl
	90	7 %	15 %	78 %	udl
	25	25 %	25 %	49 %	1 %
SBain	2.5	0	0	100%	0
	1	0	not evaluable		
	0.25	0	93 %	0	7 %
	0.05	2 %	84 %	0	14 %

6.2 Q&P and Bainitic Heat Treatments

All cooling rates of the AFP steel show multiple phase formations. Therefore, cooling rates of 90 K/s and 25 K/s have been chosen for further investigations. In addition, quenching with 120 K/s is not commercially realizable.

Furthermore, for the SBain 2.5 K/s has been chosen for further processing, as a pure martensitic transformation can be achieved for Q&P treatments and process time is kept acceptable.

Bainitic heat treatments were conducted with the intention to obtain bainitic microstructures. Thus, in following these treatments will be termed as bainitic treatments even tough other phases such as ferrite or martensite might be present.

6.2.1 Selection of Heat Treatment Parameter According to Cooling Behavior

To increase both, strength and ductility of the materials, Q&P processes and bainitic processes were chosen, considering the received information from the cooling experiments.

Applying the lever rule on the dilatometer data of the cooling rates enables an estimation of possible amounts of defined phases. The lever rule (Equ. 10) was used to determine certain amounts of martensite and austenite. Possible fractions of other phases than martensite obtained by observation of microstructure were deducted from the total amount of austenite before applying the lever rule on the characteristic length change for martensite in the dilatometer curve.

The maximum content of carbon soluble in fcc and bcc for defined fractions of austenite and martensite have been calculated with Equ. 6 - 9 of the constrained paraequilibrium. With Equ. 1 the diffusion path according to the random walk model, i.e. the distance that carbon is able to diffuse in FCC during partitioning or bainitic transformation, has been calculated. D_0 was calculated with MatCalc with the compositions of the AFP steel and the SBain, respectively. A benchmark of 500 nm as reference value has been set as minimal diffusional path to stabilize retained austenite by adjustment of partitioning temperature and time, as retained austenite during Q&P and bainitic processing appears as fine films in sub micrometre size or blocks of several micrometres [67].

The calculated parameters for Q&P treatments and the predicted amounts of retained austenite for the AFP specimens are illustrated by Table 9 and the parameters for the SBain

are displayed by Table 10. The quenching temperature is indicated by QT, the quenching rate by QR, the partitioning temperature by PT, the partitioning time by Pt, holding before reheating by t_h, the reheating rate by $\dot{t}_{reheat}$ and the cooling rate to room temperature by $\dot{t}_{end}$ for both steels. Furthermore, the diffusional path of carbon in FCC is termed as x_C and lies between 12 and 532 nm and the possible amount of carbon soluble in austenite is χ_C^{γ} with a maximum of 3.7 wt%. Fractions of retained austenite indicated by γ between 4 and 28% of both steels were determined through calculation by applying the lever rule on dilatometer data of the chosen cooling rates (QR90, QR25 of chapter 6.1.2 and QR2.5 of chapter 6.1.3) and adding XRD measurements. Therefore, the added fraction of retained austenite determined by XRD is 0% for the AFP steel and 6% for the SBain. All AFP specimens were austenitized at 850°C and the SBain specimen were austenitized at 960°C for 30 minutes. Heating and the final quench to room temperature were performed with 2 K/s. The new carbon rich austenite caused by Q&P treatments is stable to room temperature after partitioning, if the temperature Ms calculated by Equ. 4 is below RT. The Ms in Table 9 and Table 10 is only a theoretical Ms temperature, as Ms temperatures lower than -273.15°C are not reachable.

Table 9: Experimental parameters for Q&P treatments of the AFP steel (T_A=850°C, $\dot{t}_{heat}$=2 K/s, t_A=30 min, t_h=10 s, $\dot{t}_{reheat}$=2 K/s, $\dot{t}_{end}$=2 K/s). The quenching temperature QT, the quenching rate QR, the partitioning temperature PT were chosen by evaluation of experimental data, while the partitioning time Pt, the diffusion path for carbon x_c, the mole fractions of carbon in austenite χ_C^{γ} and the martensite start temperature Ms were calculated by simulation. The calculated fraction of retained austenite γ results from a combination of simulation and XRD measurements.

QT [°C]	QR [K/s]	PT [°C]	Pt [s]	x_C [nm]	χ_C^{γ} [wt%]	γ [%]	Ms [°C]
260	90	260	600	18	3.14	9	-644
260	90	300	600	55	3.14	9	-644
260	90	300	1200	78	3.14	9	-644
260	90	350	600	188	3.14	9	-644
260	90	400	600	532	3.14	9	-644
100	25	300	600	55	1.90	16	-203
300	25	300	600	55	3.00	4	-594
300	25	400	600	532	3.00	4	-594

Table 10: Experimental parameters for Q&P treatments of the AFP steel (T_A=960°C, $\dot{t}_{heat}$=2 K/s, t_A=30 min, t_h=10 s, $\dot{t}_{reheat}$=2 K/s, $\dot{t}_{end}$=2 K/s). The quenching temperature QT, the quenching rate QR, the partitioning temperature PT were chosen by evaluation of experimental data, while the partitioning time Pt, the diffusion path for carbon x_c, the mole fractions of carbon in austenite χ_C^{γ} and the martensite start temperature Ms were calculated by simulation. The calculated fraction of retained austenite γ results from a combination of simulation and XRD measurements.

QT [°C]	QR [K/s]	PT [°C]	Pt [s]	x_C [nm]	χ_C^{γ} [wt%]	γ [%]	Ms [°C]
225	2.5	350	600	180	3.7	13	-849
250	2.5	250	600	12	1.7	22	-138
250	2.5	350	600	180	1.7	22	-138
250	2.5	400	600	515	1.7	22	-138
260	2.5	350	600	180	1.2	28	38

Table 11 and Table 12 show the parameters of bainitic heat treatments for the AFP and the SBain. Bainite formation appears between 680°C and 420°C for the AFP and between 480°C and 324°C for the SBain. Hence, a QT of 450°C for the AFP and a QT of 350°C, 400°C and 450°C for the SBain are chosen. Thereby, a theoretical diffusional path x_c between 255 nm and 2969 nm is reachable according to calculations by MatCalc. The velocity of continuous cooling between 450 and 330°C of the SBain is indicated by $\dot{t}_{cool}$ in Table 12. Furthermore, the end of continuous cooling at 330°C is indicated by to.

Table 11: Experimental parameter for isothermal bainitic heat treatments of the AFP steel (T_A=850°C, $\dot{t}_{heat}$=2 K/s, t_A=30 min, $\dot{t}_{end}$=2 K/s). The quenching temperature QT, the quenching rate QR, the partitioning temperature PT were chosen by evaluation of experimental data, while the partitioning time Pt and the diffusion path for carbon x_c were calculated by simulation.

QT [°C]	QR [K/s]	PT [°C]	Pt [s]	x_C [nm]
450	25	450	600	1304
450	90	450	600	1304

Table 12: Experimental parameter for isothermal and continuous bainitic heat treatments of the SBain steel (T_A=960°C, $\dot{t}_{heat}$=2 K/s, t_A=30 min, $\dot{t}_{end}$=2 K/s). The quenching temperature QT and the quenching rate QR were chosen by evaluation of experimental data, while the partitioning time Pt, the velocity of continuous cooling $\dot{t}_{cool}$, the end of continuous cooling to and the diffusion path for carbon x_c were calculated by simulation.

QT [°C]	QR [K/s]	Pt [s]	$\dot{t}_{cool}$ [K/s]	to [°C]	x_C [nm]
350	2.5	1200	/	/	255
400	2.5	1200	/	/	728
450	2.5	1200	/	/	1800
450	2.5	/	0.05	330	1328
450	2.5	/	0.01	330	2969

6.2.2 **Phase Transformation during Q&P Treatments**

In this chapter, the results of the selected parameters on microstructure of the Q&P treatments listed in Table 9 and Table 10 are illustrated. Experimental data are edited graphically and the microstructure was analyzed by microscopy for the AFP steel and the SBain steel.
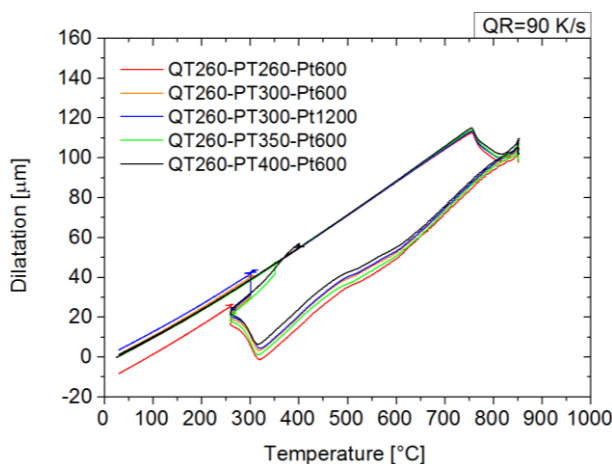

Fig. 60: Dilatation in dependence of temperature of Q&P treatments - quenched with 90 K/s of the AFP steel.

Fig. 61: Dilatation in dependence of temperature of Q&P treatments - quenched with 25 K/s of the AFP steel. All specimens were partitioned for a time of 600s.
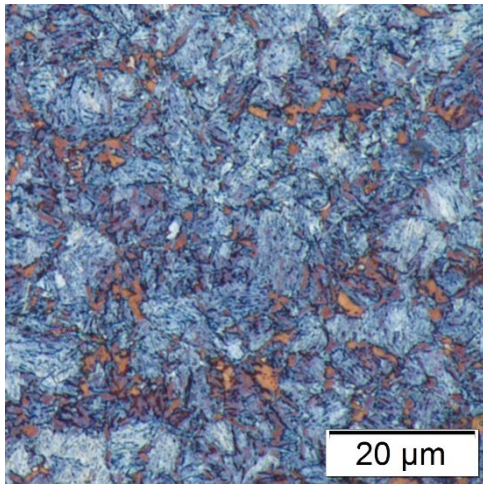
Fig. 62: Microstructure colour etched according to Klemm of the AFP steel (QR90, QT260, PT260, Pt600).
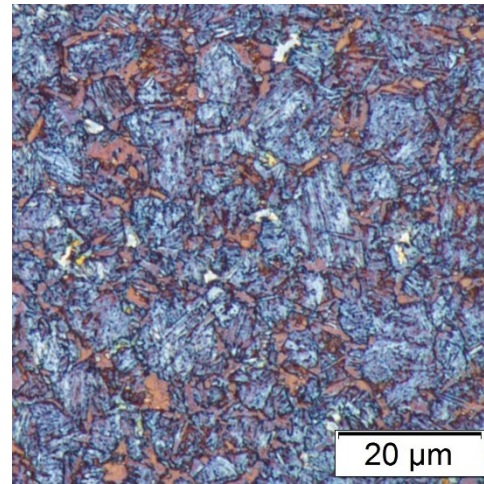
Fig. 63: Microstructure colour etched according to Klemm of the AFP steel (QR90, QT260, PT300, Pt600).
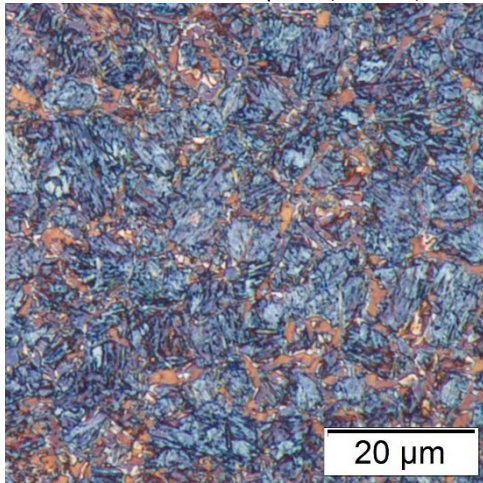
Fig. 64: Microstructure colour etched according to Klemm of the AFP steel (QR90, QT260, PT300, Pt1200).
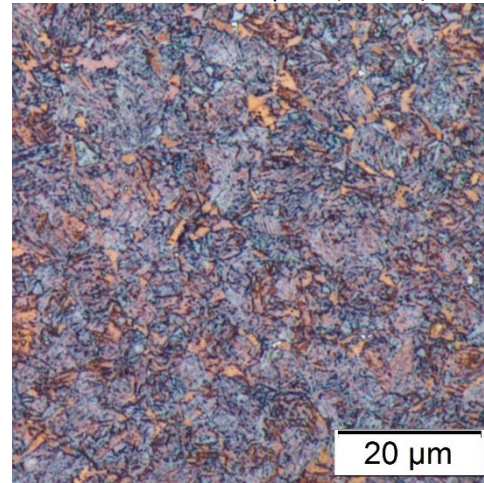
Fig. 65: Microstructure colour etched according to Klemm of the AFP steel (QR90, QT260, PT350, Pt600).
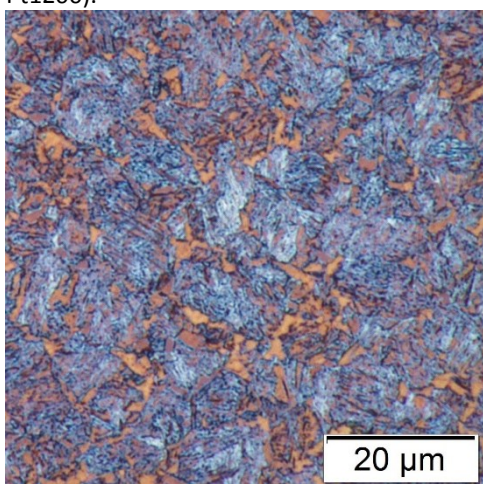
Fig. 66: Microstructure colour etched according to Klemm of the AFP steel (QR90, QT260, PT400, Pt600).
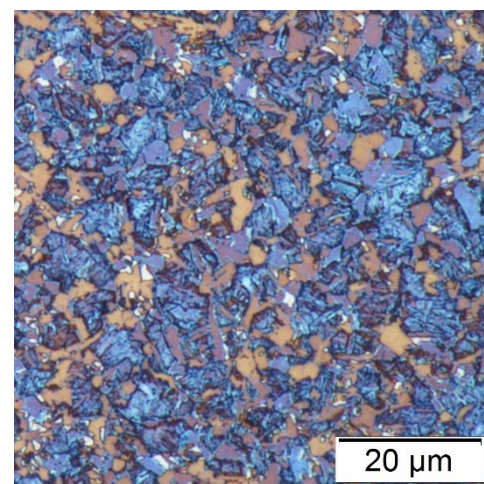
Fig. 67: Microstructure colour etched according to Klemm of the AFP steel (QR25, QT100, PT300, Pt600).
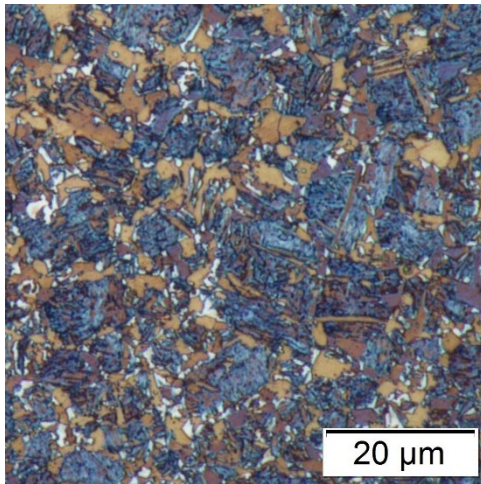
Fig. 68: Microstructure colour etched according to Klemm of the AFP steel (QR25, QT300, PT300, Pt600).
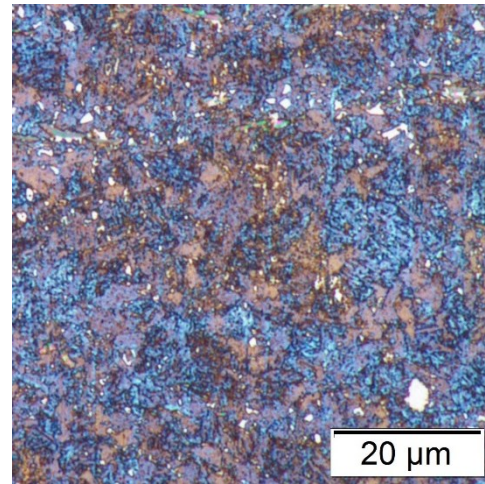
Fig. 69: Microstructure colour etched according to Klemm of the AFP steel (QR25, QT300, PT400, Pt600).

Fig. 60 shows the data of the dilatometer tests for the AFP steel quenched with 90 K/s and the data for quenching with 25 K/s are depicted in Fig. 61. As demonstrated by chapter 6.1.1, the formation of austenite during heating occurs at temperatures between 700°C and 800°C. For both cooling rates, changes in length during cooling at temperatures higher than 400°C are caused by ferrite and bainite formation. The martensite transformation starts at around 315°C and is aborted at 260°C for quenching with 90 K/s. As predicted by the cooling experiments Ms temperature is around 338°C for quenching with 25 K/s. The martensite transformation is aborted at 300°C and 100°C for the samples cooled with 25 K/s. Subsequently, all specimens (QR=90 K/s and QR=25 K/s) obtain the specific partitioning treatment at temperatures between 260°C to 400°C for 600s or 1200s.

Fig. 62 to Fig. 69 show the microstructure belonging to the respective dilatometer data of the AFP steel quenched with 90 K/s and 25 K/s. The microstructure consists of fractions of ferrite, bainite, martensite and retained austenite. Ferrite appears light brown or violet with no substructure, in blocky shape and clearly delineated to the remaining microstructure. Needle shaped bainite occurs dark brown. The light and dark blue needle shaped structure is martensite. Positions that were not etched and thus appear white are austenite or carbides.

As austenite plays an important role for ductility in this thesis, fractions of retained austenite have been determined by XRD. Q&P treatments that obtain the microstructure of QR90-QT260-PT260-Pt600, QR90-QT260-PT300-Pt600, QR90-QT260-PT350-Pt600, QR90-QT260-PT400-Pt600 and QR25-QT300-PT400-Pt600 (Fig 62, 63, 65, 66 and 69) have a fraction of retained austenite of lower than 1 %. The amount of retained austenite of QR90-QT260-PT300-Pt1200 (Fig. 64) has been determined with 7.4 ± 1 %. The microstructure of QR25-QT100-PT300-Pt600 (Fig. 67) has 4.5 ± 1 % and QR25-QT300-PT300-Pt600 (Fig. 68) has 5.5 ± 1 % of retained austenite.
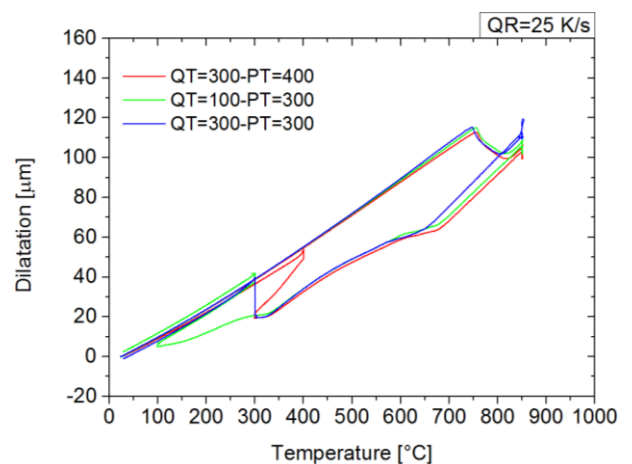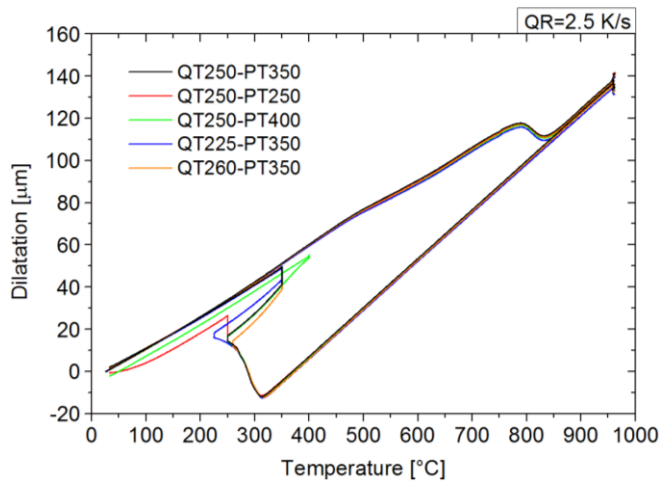
Fig. 70: Dilatation in dependence on temperature of Q&P treatments - quenched with 2.5 K/s of the SBain. All specimens obtained a partitioning time of 600s.

Fig. 71: Microstructure colour etched according to Klemm of the SBain (QT225, PT350, Pt600).

Fig. 72: Microstructure colour etched according to Klemm of the SBain (QT250, PT250, Pt600).

Fig. 73: Microstructure colour etched according to Klemm of the SBain (QT250, PT350, Pt600).

Fig. 74: Microstructure colour etched according to Klemm of the SBain (QT250, PT400, Pt600).

Fig. 75: Microstructure colour etched according to Klemm of the SBain (QT260, PT350, Pt600).

Achieved data of Q&P treatments from the dilatometer for the SBain quenched with 2.5 K/s are demonstrated by Fig. 70. Transformation of initial microstructure to austenite occurs between 780°C and 850°C (see also chapter 6.1.2). The martensite transformation starts at 324°C and is interrupted at different quenching temperatures (225°C, 250°C, 260°C), followed by the partitioning treatment. All specimens underwent the specific partitioning temperature (250°C, 350°C, 400°C) for 600s.

The respective microstructures of the dilatometer data are illustrated by Fig. 71 to Fig. 75. The needle shaped structure in blue and brown is martensite, surrounded by fractions retained austenite in white.

The amount of retained austenite of the Q&P treatment that achieve the microstructure of QT225-PT350-Pt600 (Fig. 71) has been determined with $11.5 \pm 1\,\%$ by XRD. The microstructure of QT250-PT250-Pt600, QT250-PT350-Pt600, QT250-PT400-Pt600 and QT260-PT350-Pt600 (Fig. 72, Fig 73, Fig. 74 and Fig. 75) contain fractions of $9.6 \pm 1\,\%$, $13.5 \pm 1\,\%$, $12.1 \pm 1\,\%$ and $10.5 \pm 1\,\%$ of retained austenite, respectively.

6.2.3 **Phase Transformation during Bainitic Heat Treatments**

This chapter involves the results of bainitic heat treatments listed in Table 11 and Table 12. In the following, the experimental data are plotted and the microstructure of specimens after processing obtained by microscopy is depicted.
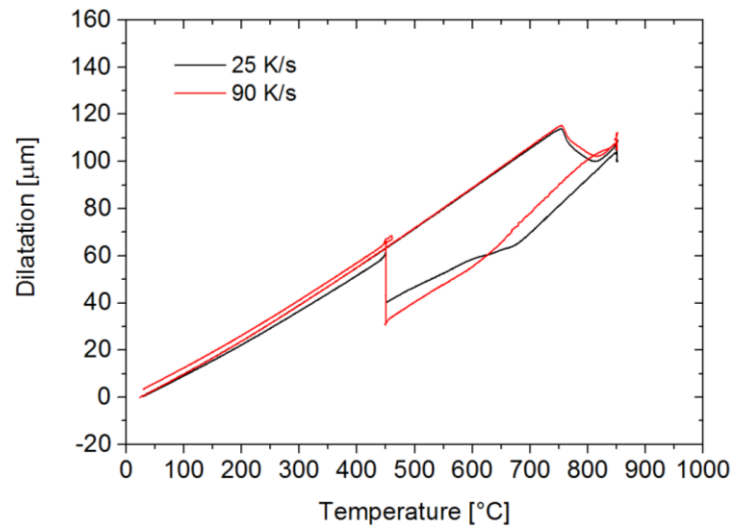
Fig. 76: Dilatation in dependence of temperature of bainitic heat treatments quenched with 90 K/s and 25 K/s of the AFP steel. QT = PT = 450°C, Pt = 600 s.
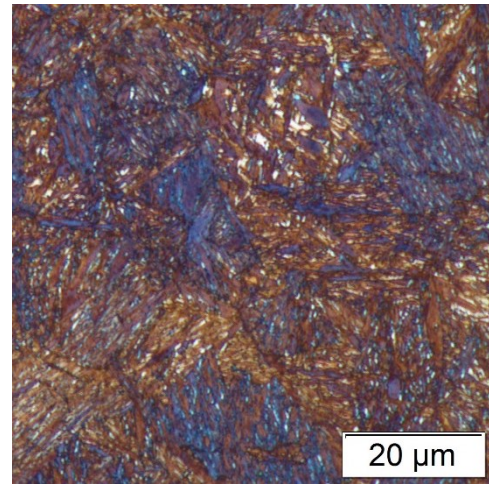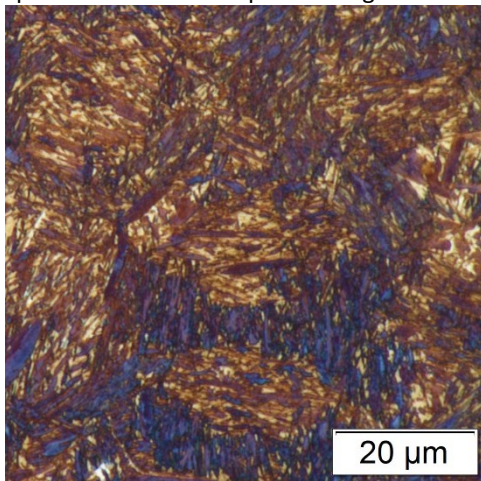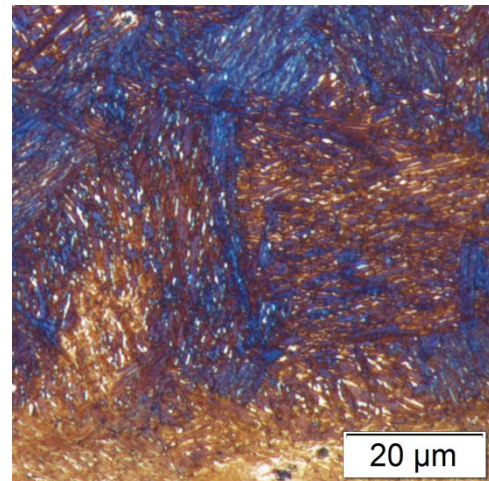

Fig. 77: Microstructure colour etched according to Klemm of the AFP steel (QR25, QT450, PT450, Pt600).
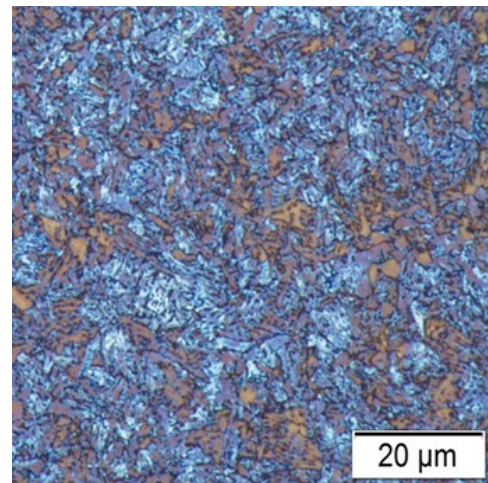
Fig. 78: Microstructure colour etched according to Klemm of the AFP steel (QR90, QT450, PT450, Pt600).

Fig. 76 illustrates the data from dilatometer measurements of bainitic heat treatments of the AFP steel quenched with 90 K/s and 25 K/s. In both cases, cooling was stopped at 450°C for 600 s, subsequently the specimens were quenched to room temperature. The deviation in slope higher than QT is caused by ferrite and beginning bainite formation (see chapter 6.1.2).

The respective microstructures of dilatometer data are depicted in Fig. 77 and Fig. 78. Ferrite appears light brown or violet with no substructure in form of blocky shaped grains. Bainite is needle shaped dark brown or blue. White areas are carbides or austenite. The specimen observed in Fig. 77 was quenched with 25 K/s and shows segregation in form of alternating lines of carbide or austenite rich fractions in the bainitic, ferritic matrix. From a purely visual point of view, the bainitic heat treatment process with a quenching rate of 90 K/s leads to ferritic, bainitic microstructure as shown in Fig. 78. Fractions lower than 1 % of retained austenite were found for both specimens by XRD.
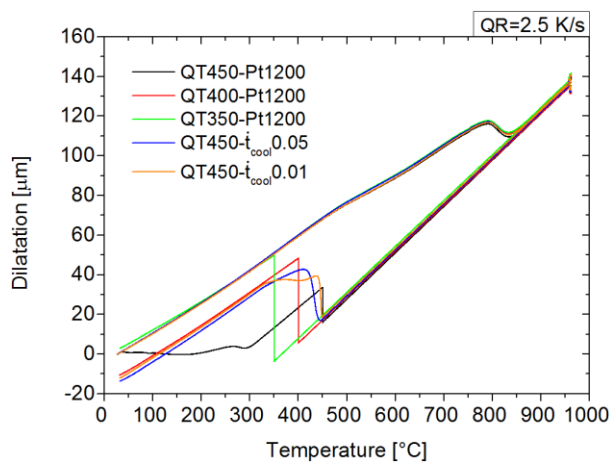
Fig. 79: Dilatation in dependence of temperature of bainitic heat treatments quenched with 2.5 K/s of the SBain.
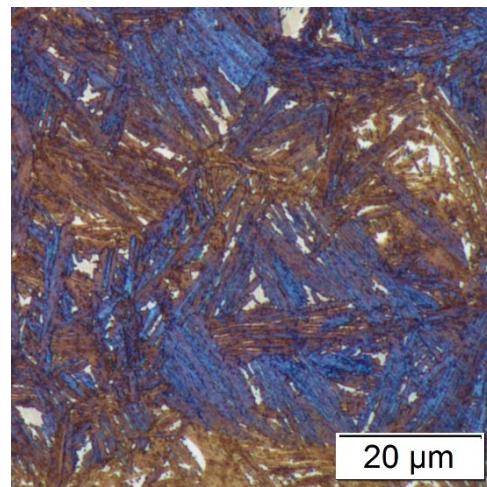
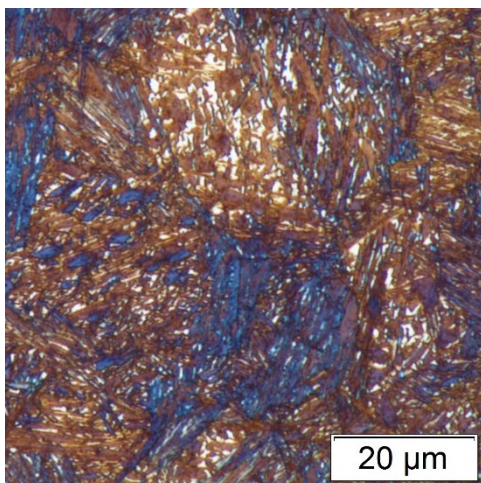Fig. 80: Microstructure colour etched according to Klemm of the SBain (QT350, Pt1200).
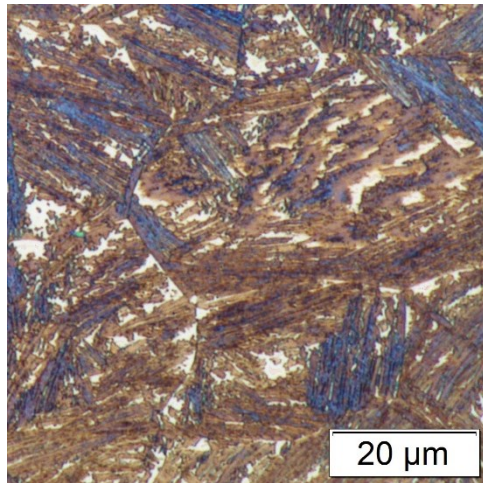
Fig. 81: Microstructure colour etched according to Klemm of the SBain (QT400, Pt1200).

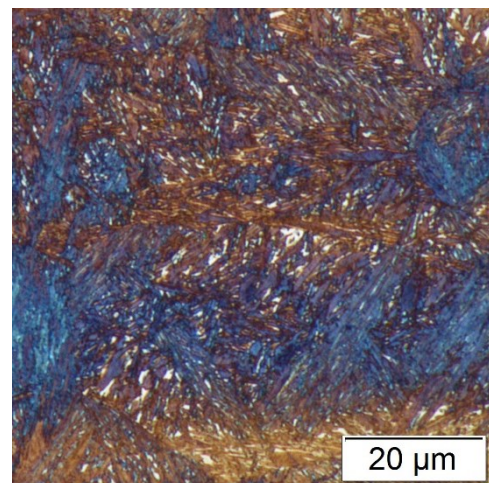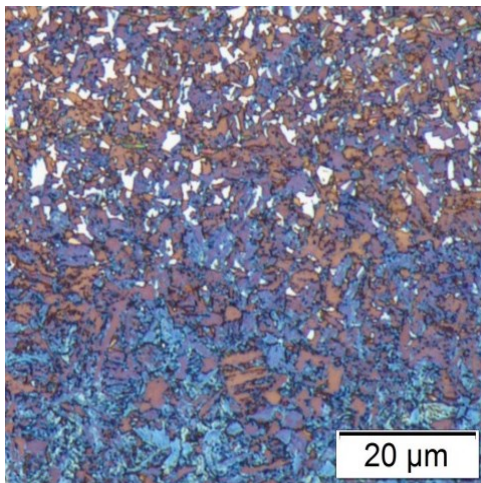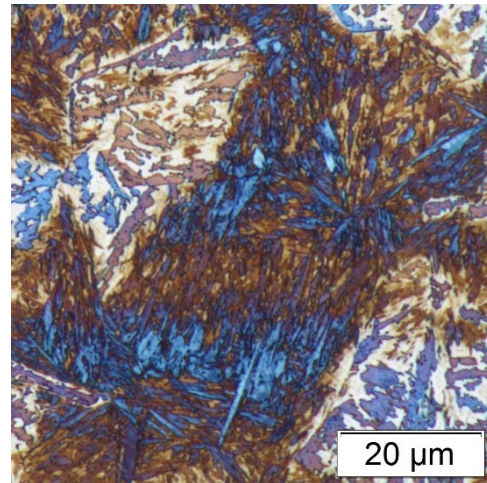Fig. 82: Microstructure colour etched according to Klemm of the SBain (QT450, Pt1200).
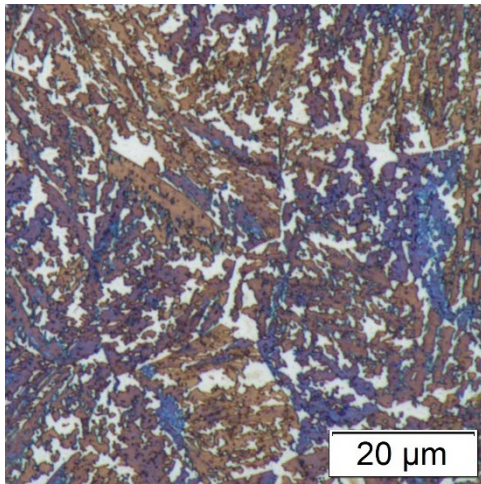
Fig. 83: Microstructure colour etched according to Klemm of the SBain (QT450, $\dot{t}_{cool}$0.05 K/s, to330).
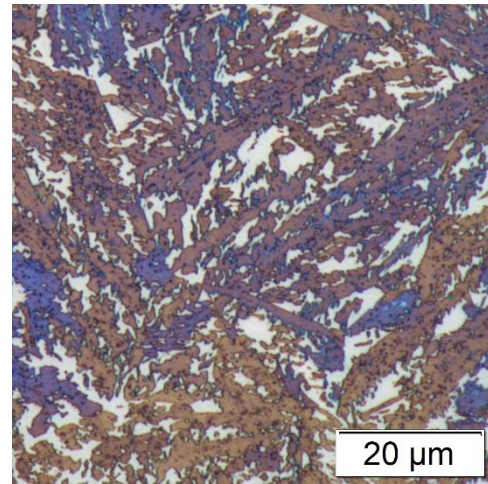
Fig. 84: Microstructure colour etched according to Klemm of the SBain (QT450°C, $\dot{t}_{cool}$0.01, to330).

The dilatometer data for bainitic heat treatments on the SBain quenched with 2.5 K/s are shown in Fig. 79. Specimens were quenched to a defined temperature and either held for 1200 s at temperature or cooled continuously with 0.05 K/s or 0.01 K/s to 330°C, followed by a final quench to room temperature. QT450-Pt1200 shows variations of length during cooling starting from 310°C. A deviation by change in length from other cooling curves around 400°C is evident at the specimen QT450-$\dot{t}_{cool}$0.01.

The microstructures obtained by microscopy are depicted in Fig. 80 to Fig. 84. Bainite is needle shaped brown and blue surrounded by fractions of retained austenite in white.

Determination of retained austenite by XRD provide fractions for the specimens depicted in Fig. 80 (QT350-Pt1200) of 10 ± 1 %, for Fig. 81 (QT400-Pt1200) of 20.8 ± 1 %, for Fig. 82 (QT450-Pt1200) of 6.2 ± 1 %, for Fig. 83 (QT450-$\dot{t}_{cool}$0.05 K/s-to330) of 25.8 ± 1 % and for Fig. 84 (QT450°C-$\dot{t}_{cool}$0.01-to330) of 25.5 ± 1 %.

6.3 Mechanical Properties

This chapter deals with the mechanical behavior of specimens after Q&P or bainitic processing. While hardness values have been determined for all specimens, tensile tests have been performed for a selection of Q&P and bainitic heat treatments that seemed confident for an improvement of mechanical properties.

Table 13 and Table 14 show the hardness according to Vickers (HV10) of the AFP and the SBain. In each case the delivery condition, Q&P treatments and bainitic heat treatments are listed, respectively.

Results of tensile testing of the AFP are listed in Table 15. Specimens that were quenched with 25 K/s to 450°C and held at temperature for 600 s or with a QR of 90 K/s, a QT and PT of 450°C and a Pt of 600 s show a pronounced yield strength. The upper and lower yield strength are indicated by R_{eH} and R_{eL}.

The results of tensile testing of the SBain are listed in Table 16. Values for simply cooling from austenitization temperature to room temperature of defined cooling rates, Q&P treatments and bainitic heat treatments are displayed. The data marked in blue indicate specimens that broke at the edge of the gauge length. These data especially A, Ag and Z serve only as an estimation to actual values.

Table 13: Hardness according to Vickers for the AFP steel.

Heat treatment condition	HV10	Heat treatment condition	HV10
As delivered	223	QR25, QT100, PT300, Pt600	330
QR90, QT260, PT260, Pt600	417	QR25, QT300, PT300, Pt600	320
QR90, QT260, PT300, Pt600	399	QR25, QT300, PT400, Pt600	287
QR90, QT260, PT300, Pt1200	410	QR25, QT450, PT450, Pt600	278
QR90, QT260, PT350, Pt600	397	QR90, QT450, PT450, Pt600	291
QR90, QT260, PT400, Pt600	366		

Table 14: Hardness according to Vickers for the SBain quenched with 2.5 K/s.

Heat treatment condition	HV10	Heat treatment condition	HV10
As delivered	396	QT350, Pt1200	485
QT225, PT350, Pt600	510	QT400, Pt1200	414
QT250, PT250, Pt600	574	QT450, Pt1200	567
QT250, PT350, Pt600	502	QT450, $\dot{t}_{cool}$0.05, to330	377
QT250, PT400, Pt600	488	QT450, $\dot{t}_{cool}$0.01, to330	359
QT260, PT350, Pt600	496		

Table 15: Results of tensile testing for the AFP steel annealed at 850°C with two specimens showing a pronounced yield strength. R_{eH} and R_{eL} indicate upper and lower yield strength.

Heat treatment condition	$R_{p0.2}$ [MPa]	Rm [MPa]	A [%]	Ag [%]	Z [%]	γ_{ret} [%]
QR90, QT260, PT300, Pt600	921	1235	11	4	49	<1
QR90, QT260, PT300, Pt1200	1015	1249	10	4	53	7.4 ± 1
QR90, QT260, PT400, Pt600	1029	1118	13	3	68	<1
QR25, QT100, PT300, Pt600	717	1122	15	10	68	4.5 ± 1
QR25, QT300, PT300, Pt600	549	1093	18	10	49	5.5 ± 1
QR25, QT450, PT450, Pt600	R_{eH}=786 R_{eL}=711	842	23	11	71	<1
QR90, QT450, PT450, Pt600	R_{eH}=770 R_{eL}=710	845	17	6	68	<1

Table 16: Results of tensile testing for the SBain annealed at 960°C. Specimens marked in blue broke outside the at the edge of the reduced length L_C.

Heat treatment condition	Rp$_{0.2}$ [MPa]	Rm [MPa]	A [%]	Ag [%]	Z [%]	γ$_{ret}$ [%]
QR0.25	888	1384	14	7	45	18.7 ± 1
QR0.05	736	1251	23	18	40	24.7 ± 1
QR2.5, QT225, PT350, Pt600	1400	1674	12	4	52	11.5 ± 1
QR2.5, QT250, PT250, Pt600	1051	2066	11	6	33	9.6 ± 1
QR2.5, QT250, PT350, Pt600	1357	1642	13	4	53	13.5 ± 1
QR2.5, QT250, PT400, Pt600	1304	1625	16	9	48	12.1 ± 1
QR2.5, QT260, PT350, Pt600	1339	1643	13	5	52	10.5 ± 1
QR2.5, QT350, Pt1200	1145	1585	13	4	60	10 ± 1
QR2.5, QT400, Pt1200	833	1416	17	12	40	20.8 ± 1
QR2.5, QT450, Pt1200	810	1540	3	3	21	6.2 ± 1
QR2.5, QT450, $\dot{t}_{cool}$0.05, to330	686	1349	20	17	45	25.8 ± 1
QR2.5, QT450, $\dot{t}_{cool}$0.01, to330	687	1276	26	20	39	25.5 ± 1

6.4 Discussion of Q&P and Bainitic Heat Treatments and their Mechanical Behavior

The fractions of retained austenite were expected to be the main influence on ductility in this thesis. Strength is mainly caused by fractions of martensite and bainite. Therefore, data obtained by dilatometer, microscopy, XRD, hardness measurements according to Vickers and tensile testing served to estimate the behavior of the AFP and SBain after thermal processing.

6.4.1 Influence of Alloying Elements on Q&P Processes and Bainitic Heat Treatments of the AFP Steel and the SBain

Different alloying element contents of two steels were examined to study their influence during thermal processing. The Mn, Mo and Cr contents are not discussed any further, as they mainly delay the transformation behavior during cooling to later times [59], which is already discussed in chapter 6.1. The V content is nearly the same for both steels. The formation of secondary carbides (e.g. MV) was not considered, as their size in the range of nm is below the resolution of the SEM. This is analogous for the detection of transition carbides.

Hence, the influence of C and Si is of interest for the following discussion. The AFP steel has a carbon content of 0.28 wt% and a silicon content of 0.58 wt%, whereas the SBain is higher in carbon and silicon content with 0.4 wt% C and 1.1 wt% Si.

Q&P processes and bainitic heat treatments were applied on both steels to stabilize distinct fractions of austenite at room temperature by carbon enrichment. Neither Q&P processes nor bainitic heat treatments applied on the AFP steel led to high contents of retained austenite, as it is shown by γ_{ret} determined by XRD and listed in Table 15. The fractions of retained austenite of the SBain listed in Table 16 are significant higher compared to those of the AFP steel and it was found that Q&P processes obtained lower fractions than bainitic heat treatments.

It is expected that the far lower γ_{ret} content of the AFP steel might be caused by the lower content of C and Si. A formation of cementite and alloy carbides is generally suppressed by alloying silicon. The Si content of the AFP steel of 0.58 wt% might be too low to impede cementite formation. Thus, as carbides work as carbon sinks less carbon was available for partitioning in austenite [3, 44]. Table 17 compares the calculated γ and experimentally determined fractions of retained austenite γ_{ret} of Q&P processes. The SBain stabilized more

austenite than the AFP, but not as much as predicted by calculation. It is suggested that at the point of beginning partitioning, the calculated fraction of retained austenite was present, which transformed during further processing, as the C available for stabilization was too low to stabilize the whole austenite.

Table 17: Comparison of calculated and determined fractions of retained austenite of Q&P Processes. The calculated and the determined amount of retained austenite are indicated by γ and γ_{ret}, respectively.

Alloy	Heat Treatment Parameter	Calculated γ [%]	Experimentally determined γ_{ret} [%]
AFP	QR90-QT260-PT260-Pt600	9	<1
	QR90-QT260-PT300-Pt600	9	<1
	QR90-QT260-PT300-Pt1200	9	7.4 ± 1
	QR90-QT260-PT350-Pt600	9	<1
	QR90-QT260-PT400-Pt600	9	<1
	QR25-QT100-PT300-Pt600	16	4.5 ± 1
	QR25-QT300-PT300-Pt600	4	5.5 ± 1
	QR25-QT300-PT400-Pt600	4	<1
SBain	QR2.5-QT225-PT350-Pt600	13	11.5 ± 1
	QR2.5-QT250-PT250-Pt600	22	9.6 ± 1
	QR2.5-QT250-PT350-Pt600	22	13.5 ± 1
	QR2.5-QT250-PT400-Pt600	22	12.1 ± 1
	QR2.5-QT260-PT350-Pt600	28	10.5 ± 1

The transformation of austenite during partitioning is also evident in Fig. 60 and Fig. 61 for the AFP steel, as well as in Fig. 70 for the SBain, as an increase of the dilatation at partitioning temperature indicates austenite to bcc and cementite transformation.

Comparing the strength and the ductility of the state of delivery and heat-treated conditions of the AFP steel (see Table 15) show that strength of the delivery state of Rm = 782 MPa has been increased up to 1249 MPa, whereby ductility represented by the elongation at fracture has been decreased (A of delivery state = 24 %, highest A of heat treatment = 23 %). The approximation of 3.5*HV10 according to DIN EN ISO 18265: 2014-02 [68] allows an estimation of the tensile strength of the initial state of the SBain with Rm = 1386 MPa. Heat treatments of the SBain (see Table 16) caused Rm values up to 2066 MPa with an elongation at fracture up to 26 %.

The following discussion specifies the behavior of the AFP steel and the SBain separately during processing.

6.4.2 Discussion of the Phase Transformation and Mechanical Properties of the AFP Steel

The microstructure of the AFP steel after Q&P processing, as demonstrated by Fig. 62 to Fig. 69, shows fractions of ferrite, bainite, martensite and austenite, which vary only slightly. The microstructure of bainitic heat treated AFP specimens (Fig. 77 and Fig. 78) is ferritic, bainitic and austenitic with similar fractions. Hence, the microstructure of each treatment is not discussed any further.

Q&P treated specimens show specific details concerning the amount of retained austenite (see Table 15). Only 3 out of 5 Q&P processes led to significant amounts of retained austenite. The parameters QR90-QT260-PT300-Pt1200 show the highest fractions of γ_{ret} with 7.4 %. This relatively high amount of γ_{ret} compared to other specimens quenched with 90 K/s is attributed to the longer partitioning time. Longer Pt offers more time for carbon partitioning, which results in higher carbon enriched austenite and higher fractions at room temperature. QR90-QT260-PT400-Pt600 obtained equally γ_{ret}<1% than QR90-QT260-PT300-Pt600 (γ_{ret}<1%), which indicates that the partitioning temperature might not have any influence on austenite stability. By comparing the quenching rates of 25 K/s, it is shown, that decreasing the quenching temperature form 300°C to 100°C results in a lower fraction of γ_{ret}. With decreasing QT, more martensite is formed and less austenite is present for the following partitioning treatment.

The examination of mechanical properties shows a clear influence of PT on strength and ductility of Q&P processes. High PT probably caused tempered martensite, which results in lower tensile strength with higher elongation at fracture. However, since both specimens with QR25 were treated with the same PT, the higher amount of γ_{ret} of QR25-QT300-PT300-Pt600 is supposed to be the reason for the lower strength and higher ductility values.

Both bainitic heat treated specimens obtained minimal fractions of retained austenite. This is due to progressive austenite to bainite transformation at QT=PT (see Fig. 76) until no austenite was left. QR90-QT450-PT450-Pt600 obtains a higher tensile strength with lower ductility than QR25-QT450-PT450-Pt600, resulting from the higher quenching rate, that probably caused harder bainite and less ferrite. Bainitic heat treatments led to lower strength values and higher ductility values than the Q&P processes with similar quenching rates, resulting from the higher amount of bainite instead of martensite.

The influence of ferrite on mechanical properties achieved by both Q&P and bainitic thermal treatments cannot be excluded, as ferrite exhibits low strength and high ductility. Hence, phase fractions of ferrite up to 25% (see chapter 6.1.2) decreases strength and enhances ductility. Furthermore, it should be mentioned that retained austenite has a minor role on

mechanical properties of the AFP steel, e.g. QR90-QT260-PT300-Pt1200 has the highest amount of γ_{ret}, as well as the highest tensile strength with the lowest elongation at fracture. QR25-QT100-PT300-Pt600 caused the best overall mechanical properties with $Rp_{0.2}$=717 MPa, Rm=1122 MPa, A=15 %, Ag=10 %, Z=68 % and γ_{ret}=4.5 ± 1 %.

6.4.3 Discussion of the Phase Transformation and Mechanical Properties of the SBain

The microstructure of the SBain after Q&P processing is demonstrated by Fig. 71 to Fig. 75 and shows fractions of martensite and retained austenite, which vary only slightly. The microstructure of bainitic heat treated SBain specimens (Fig. 80 to Fig. 84) is bainitic and austenitic with similar fractions.

All Q&P processes caused nearly the same fractions of retained austenite between 9.6 % and 13.5 % (see Table 16), regardless of quenching temperature. De Moor et al. [44] showed that retained austenite is not sensitive to QT. Whereas QT only sets the initial fraction of austenite to be stabilized, the partitioning temperature and time are more related to austenite stability, as carbon enrichment of austenite takes place during partitioning treatment. If different processes have nearly the same PT and Pt, similar carbon enrichment of the initial fraction of austenite can be expected. Austenite with insufficient carbon enrichment might transform to bcc with or without formation of cementite. This is also evident in the dilatometer curves of Fig. 70 with an elongation at holding at PT.

The PT of Q&P processes shows an influence on strength and ductility. High PT increases the tempering of martensite and raises the fraction of stabilized austenite, which is apparent in lower tensile strength with higher elongation at fracture. Furthermore, specimens treated with QR2.5-QT225-PT350-Pt600, QR2.5-QT250-PT350-Pt600 and QR2.5-QT260-PT350-Pt600 achieved nearly the same mechanical properties, which indicates that QT has no influence on strength and ductility. The highest tensile strength of 2066 MPa of QR2.5-QT250-PT250-Pt600 might be formation of untempered martensite during final cooling and is evident in Fig. 70 by a change in length at around 100°C as well as the lowest fraction of retained austenite of 9.6 ± 1 %

High fractions of retained austenite of the SBain were attainable by bainitic heat treatments. The growth of a bcc subunit during bainite formation generates a bcc plate. Subsequently carbon is partitioned to the surrounding austenite. Progressive bainite formation leads to enrichment of austenite with more and more carbon. The precipitation of carbon in form of carbides should be supressed by the Si content as mentioned in chapter 6.4.1. The specimen

QR2.5-QT450-Pt1200 shows the lowest fraction of retained austenite of 6.2 %, which might be caused by a fraction of austenite which is too high to enable a sufficient enrichment with carbon during the isothermal partitioning treatment at 450°C and a time of 1200 s. This is evident in the change of length at around 300°C of the specimen's dilatometer curve (see Fig. 79), which might be attributed to austenite transformation to martensite, as well as in high strength and low ductility values. On the contrary, QR2.5-QT350-Pt1200 obtained an amount of retained austenite comparable to Q&P processes. This effects the mechanical properties, which are also similar to Q&P processes. Bainitic heat treatments with continuous cooling caused the highest fractions of retained austenite. Continuous cooling from 450°C to 330°C with a cooling rate of 0.05 K/s or 0.01 K/s means partitioning times of 2400 s and 12000 s, respectively. Hence, the specimens QR2.5-QT450-$\dot{t}_{cool}$0.05-to330 and QR2.5-QT450-$\dot{t}_{cool}$0.01-to330 had enough time to enrich the austenite with carbon. This resulted in lower strength with the highest overall achieved ductility values of all thermal treatment parameters.

In summary, Q&P processes achieved high strength with low ductility and nearly the same fractions of retained austenite, which indicates that the variation of Q&P parameters has a minor role on austenite phase fraction and mechanical properties. Bainitic heat treatments caused a combination of high strength and high elongation, with austenite phase fractions up to 26 % influencing mechanical properties. Table 18 lists the parameters of thermal treatments of the SBain that achieved the best overall mechanical values.

Table 18: Heat treatments of the SBain that obtained an improvement in overall mechanical behavior.

Heat treatment condition	$Rp_{0.2}$ [MPa]	Rm [MPa]	A [%]	Ag [%]	Z [%]	γ_{ret} [%]
QR0.05	736	1251	23	18	40	24.7 ± 1
QR2.5, QT400, Pt1200	833	1416	17	12	40	20.8 ± 1
QR2.5, QT450, $\dot{t}_{cool}$0.01, to330	687	1276	26	20	39	25.5 ± 1

6.5 Concluding Remarks and Future Prospects

This work focused on the increase of strength and ductility of low alloyed cold forging steels. Therefore, two alloys the AFP a 30MnVS6 grade and the SBain have been chosen. The initial state of the AFP has a pearlitic, ferritic microstructure with a tensile strength of 782 MPa and an elongation at fracture of 24 %, while the intitial microstructure of the SBain is bainitic and hardness according to Vickers was determined with 396HV10. In addition, both steels should improve their mechanical behavior by applying specific thermal treatments. Furthermore, fractions of retained austenite at room temperature should be compared.

The analysis of the behavior during cooling served to gain a fundamental knowledge of transformation kinetics of each alloy to be able to choose suitable parameters for Q&P and bainitic heat treatments. The parameters controlling the strength of Q&P processes are the fractions of martensite and the fractions of bainite for bainitic heat treatments. In addition, the ductility for both processes is decisively affected by the amount of retained austenite. For the AFP steel multiple phase transformations during cooling appeared even at quenching with 120 K/s, which made it impossible to obtain pure martensite. Thus, quenching with 90 K/s and 25 K/s have been chosen for further processing. Transformation of the SBain is shifted to longer times which led to pure martensite transformation at a quenching rate of 2.5 K/s.

Neither Q&P processes nor bainitic heat treatments applied on AFP specimens led to high fractions of retained austenite, whereas the SBain obtained significant higher fractions of retained austenite due to processing. This might be related to the higher content of Si of the SBain, which suppressed cementite formation during the partitioning treatment. Q&P processes led to higher tensile strength values and lower elongation at fracture values than the delivery condition of the AFP steel, whereas bainitic heat treatments realized higher strength values with elongation values comparable to the delivery condition. Due to the low fractions of retained austenite, it can be presumed that austenite has a minor role on ductility of the AFP steel. SBain specimens with Q&P treated conditions obtained nearly the same fractions of retained austenite with an increase in strength compared to the delivery condition, but low ductility values. It was shown that with bainitic heat treatments of the SBain, high fractions of retained austenite were stabilized. The tensile strengths were lower than those of Q&P treated specimens, but even the highest overall elongation at fracture around 26 % was achievable by bainitic heat treatments of the SBain. Fig. 85 demonstrates an Ashby map with conventional low alloyed and AHSS grades. The tensile strength and the elongation at fracture of Q&P Processes as well as bainitic heat treatments applied on AFP

and SBain specimens are marked by colored triangles. Bright blue and bright green triangles represent Q&P Processes of the AFP steel and the SBain, respectively. Bainitic heat treatments of the AFP steel and the SBain are indicated by dark blue and dark green triangles, respectively. It is evident that the AFP specimens obtained values that do not reach the area of current third generation AHSS. However, SBain specimens are located in the area of third generation AHSS.
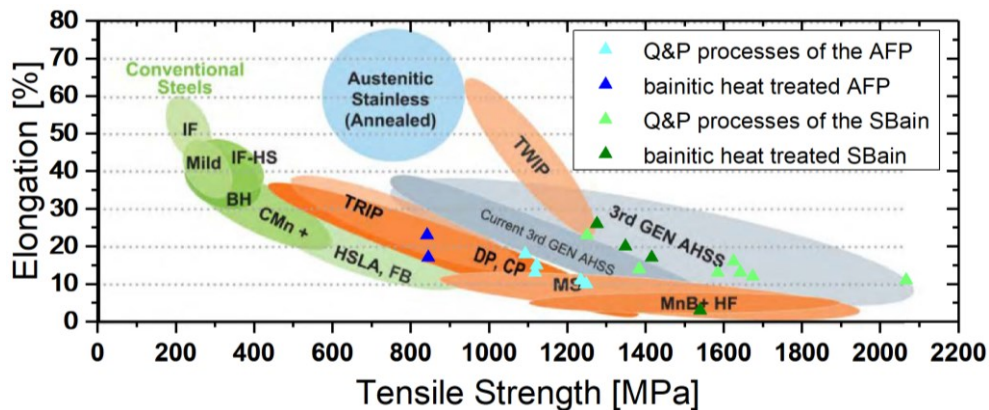

Fig. 85: Ashby map representing the strength–ductility relationship of various conventional and AHSS grades [3]. Tensile strength and elongation at fracture of Q&P and bainitic heat treated AFP and SBain specimens are marked by colored triangles.

Further tensile tests of the initial state and heat-treated states must be carried out to obtain a more accurate statement about the increase of strength and ductility due to heat treatments in future. Possible combinations of treatment parameters to improve individual mechanical values should be investigated. Consequently, a combination of the process parameters of the SBain of QR2.5-QT400-Pt1200 and QR2.5-QT450-$\dot{t}_{cool}$0.01-to330 to QR2.5-QT400-$\dot{t}_{cool}$0.01-to330 may accomplish better mechanical values. As it was shown that the lower QT of bainitic heat treatments results in higher strength, as well as continuous cooling leads to high elongation values, an ideally result of Rm of 1416 MPa and Rp$_{0.2}$ of 833 MPa with a A of 26 % and a Ag of 20 % might be achievable.

Moreover, other alloys, whose compositions are tailored to Q&P and bainitic heat treatments, should be investigated. Also of interest are other heat treatments, e.g. one promising way would be thermomechanical processing. Furthermore, the determination of carbon enrichment in austenite should be considered as the carbon content is relevant for austenite stability.

Bibliography

[1] M. S. Agerer, „Maschinenbau-Wissen," 2009. [Online]. Available: http://www.maschinenbau-wissen.de/skript3/mechanik/festigkeitslehre/159-festigkeit. [Zugriff am 5 august 2017].

[2] W. Bergmann, Werkstofftechnik 1: Struktureller Aufbau von Werkstoffen - Polymerwerkstoffe - Nichtmetallisch - anorganische Werkstoffe, München: Carl Hanser Verlag, 2013.

[3] M. I. de Diego Calderón, Mechanical properties of advanced high-strenght steels produced via Quenching and Partitioning, Madrid: Universidad Carlos III de Madrid, 2015.

[4] D. K. Matlock und J. G. Speer, *Processing Oppertunities for New Advanced High-Strength Sheet Steels,* Taylor & Francis Group, LLC, 2010.

[5] P. Shewmon, Diffusion in Solids: Second Edition, Cham: Springer, 2016.

[6] I. L. Mostinsky, „Thermopedia, DIFFUSION COEFFICIENT," begell, 2 February 2011. [Online]. Available: http://www.thermopedia.com/content/696/. [Zugriff am 6 August 2017].

[7] R. Labie, W. Ruythooren und J. Van Humbeeck, *Solid state diffusion in CueSn and NieSn diffusion couples with flip-chip scale dimensions,* Leuven: Elsevier, 2006.

[8] J. G. Speer, F. C. R. Assunçãob, D. K. Matlocka and D. V. Edmonds, "The "Quenching and Partitioning" Process: Background and Recent Progress," *Materials Research,Vol. 8,No. 4,* pp. 417-423, 8 April 2005.

[9] H. K. Yeddu, *Martensitic Transformations in Steels,* Sweden: KTH Industrial Engineering and Management, 2012.

[10] A. Saxena, S. Prasad, S. Goswami, J. Subudhi und S. Chaudhuri, *Influence of austempering parameters on the microstructure and tensile properties of a medium carbon–manganese steel,* ELSEVIER, 2006.

[11] K. P. Shah, „Practical Maintenance," [Online]. Available: http://practicalmaintenance.net/?p=1315. [Zugriff am 14 April 2017].

[12] D. Kopeliovich, „SubsTech: Iron-carbon phase diagram," SubsTech, april 2007. [Online]. Available: http://www.substech.com/dokuwiki/doku.php?id=iron-carbon_phase_diagram. [Zugriff am 3 August 2017].

[13] H. J. Bargel und G. Schulze, Werkstoffkunde, Berlin-Heidelberg: Springer, 2008.

[14] D. Ponge, „C.A.T.S. - Centrum für Angewandte Technologie Werkstoffe - Umwelt,“ [Online]. Available: https://hs-flensburg.de/wt/metalle2.html. [Zugriff am 18 04 2017].

[15] R. Bürgel, Handbuch Hochtemperatur-Werkstofftechnik: Grundlagen, Werkstofbeanspruchungen, Hochtemperaturlegierungen und - beschichtungen, Springer - Verlag, 2006.

[16] W. Weißbach, Werkstoffkunde: Strukturen, Eigenschaften, Prüfung, Springer Science & Business Media, 2007.

[17] J. M. HYZAK und I. M. BERNSTEIN, „The Role of Microstructure on the Strength and,“ *Metallurgical Transactions A,* p. 1217–1224, August 1976.

[18] Edelstahl-Vereinigung e. V. mit Verein Deutscher Eisenhüttenleute, Nichtrostende Stähle. 2., neubearbeitete Auflage, Düsseldorf: Verlag Stahleisen mbH, 1989.

[19] C. Müller-Bollenhagen, *Verformungsinduzierte Martensitbildung bei mehrstufiger Umformung und deren Nutzung zur Optimierung der HCF- und VHCF-Eigenschaften von austenitischen Edelstählen,* Siegen: Department Maschinenbau an der Fakultät IV, Universität Siegen, 2011.

[20] J. Wang und S. Zwaag, „Stabilization mechanisms of retained austenite in transformationinduced,“ in *Metallurgical and Materials Transactions A,Vol. 32 (2001), Nr 6, S 1527-1539*, 2001.

[21] G. Lacroix und T. J. P. Pardoen, *The fracture toughness of TRIP-assisted multiphase steels.,* Acta Materialia, Vol. 56 (2008), Nr. 15, S. 3900-3913, 2008.

[22] H. K. D. H. Bhadeshia, „Atomic mechanism of the bainite transformation,“ in *Bainite - from nano to macro*, Wiesbaden, 2017.

[23] C. Garcia-Mateo and F. G. Caballero, *Adcanced High Strength Bainitic Steels,* Madrid: Elsevier Ltd., 2014.

[24] W. D. J. Callister und D. G. Rethwisch, Materialwissenschaften und Werkstofftechnik: Eine Einführung, Windheim: Wiley-VCH Verlag & Co. KGaA, 2013.

[25] H. K. D. H. Bhadeshia und D. V. Edmonds, *The Bainite Transformation in a Silicon Steel,* Metallurgical Transaction A, 1979.

[26] L. Fielding, *The Bainite Controversy,* Department of Materials Science and Metallurgy, University of Cambridge, 2013.

[27] H. K. D. H. Bhadeshia, *Martensite and Bainite in Steels : Transformation,* Cambridge: HAL archives - ouvertes.fr, 1997.

[28] J. e. a. KIRKALDY, *Prediction of Microstructure and Hardenability in Low Alloy Steels,* Philadelphia: Phase Transformations in Ferrous Alloys, AIME, 1983,.

[29] A. A. Gorni, Steel Forming and Heat Treating Handbook, São Vicente, 2016.

[30] H. K. D. H. Bhadeshia, Bainite in Steels - Transformations, Microstructure and Properties (Second Edition), London: Institude of Materils Communications Ltd, 2001.

[31] H. K. D. H. Bhadeshia, „Interpretation of the Microstructure of Steels," University of Cambridge, [Online]. Available: https://www.phase-trans.msm.cam.ac.uk/2008/Steel_Microstructure/SM.html. [Zugriff am 01 September 2017].

[32] Z. Nishiyama, Martensitic Transformation, New York: Academic Press, Inc., 1978.

[33] H. K. D. H. Bhadeshia, Worked examples in the Geometry of Crystals: Seond Edition, London: Institute of Materials, 2001.

[34] G. Krauss, *Martensite in steel: strength and structure,* Elsevier Science S.A., 1999.

[35] B. Fromme, *Schallgeschwindigkeit in Metallen – Messung mit Cassy,* Fakultät für Physik, Universität Bielefeld.

[36] „LD Didactic," [Online]. Available: https://www.ld-didactic.de/software/524221de/Content/ExperimentExamples/Physics/Mechanics/VelocitySoundSolids.htm. [Zugriff am 17 May 2017].

[37] K. E. Easterling und A. Thölèn, *On the Groth of Martensite in Steel,* Great Britain: Pergamon Press, 1980.

[38] J. Kundrák, Z. Gácsi, K. Gyáni, V. Bana und G. Tomolya, *X-ray diffraction investigation of white layer development,* London: Springer-Verlag , 2011.

[39] C. a. Liu, *A New Empirical Formula for Ms Temperature in Pure Iron and Ultra Low Carbon Alloy.,* Journal of Materials Processing Technology, 2001.

[40] H. S. Yang und H. K. D. H. Bhadeshia, *Austenite grain size and the martensite-start temperature,* Elsevier, 2008.

[41] H. S. Yang, D. W. Suh und H. Bhadeshia, *More Complete Theory for the Calculation of the Martensite-Statrt Temperature in Steels,* ISIJ International, 2012.

[42] B. C. De Cooman, S. Jong Lee, S. Shin, E. Jung Seo und J. G. Speer, *Combined Intercritical Annealing and Q&P Processing of Medium Mn Steel,* The Minerals, Metals & Materials Society and ASM, 2016.

[43] E. P. Bagliani, M. J. Santofimia, L. Zhao, J. Sietsma und E. Anelli, *Microstructure,tensileandtoughnesspropertiesafterquenching,* Elsevier , 2012.

[44] E. De Moor, S. Lacroix, A. J. Clarke, J. Penning und J. G. Speer, *Effect of Retained Austenite Stabiliyed via Quench and Partitioning on the Strain Hardening of Martensitic Steels,* The Minerals, Metals & Materials Society and ASM International, 2008.

[45] E. De Moor, J. G. Speer, D. K. Matlock, J. H. Kwak und S. B. Lee, „Effect of Carbon and Manganese on the Quenching and," Bd. Vol.51, Nr. 1, pp. 137-144, 2010.

[46] H. Liu, X. Lu, X. Jin, H. Dong und J. Shi, *Enhanced mechanical properties of a hot stamped advanced high-strength steel treated by quenching and partitioning process,* Shanghai: Elsevier, 2010.

[47] M. Karam-Abian, A. Zarei-Hanzaki, H. R. Abedi und S. Heshmati-Manesh, *Microandmacro-mechanicalbehaviorofatransformation-induced plasticity steel developed by thermomechanical processing followed by quenching and partitioning,* Teheran: Elsevier, 2015.

[48] D. K. Matlock, V. E. Bräutigam und J. G. Speer, *Application of the Quenching and Partitioning (Q&P) Process to a Medium-Carbon, High-Si Microalloyed Bar Steel,* Trans Tech Publications, Switzerland, 2003.

[49] J. G. Speer, E. De Moor and A. J. Clarke, *Critical Assessment 7: Quenching and partitioning,* Taylor and Francis Group, 2014.

[50] H. Jiang, B. Zhuang, X. Duan, Y. Wu und Z. Cai, *Element distribution and diffusion behavior in Q&P steel during,* Beijing: International Journal of Minerals, Metallurgy andMaterials, 2013.

[51] G. A. Thomas, J. G. Speer und D. K. Matlock, *Quenched and Partitioned Microstructures Produced via,* The Minerals, Metals & Materials Society and ASM International, 2011.

[52] R. Wu, X. Jin, C. Wang und L. Wang, *Effect of annealing on Microstructural Evolution and Properties of Quenching & Partitioned (Q&P) Steels,* ASM international, 2015.

[53] M. Hillert und J. Ågren, *Reply to comments on ''On the definition of paraequilibrium and orthoequilibrium'',* ELSEVIER, 2014.

[54] J. Cao, J. Yan, J. Zhang und T. Yu, *Effects of thermomechanical processing on microstructure and properties of bainitic work hardening steel,* Elsevier, 2015.

[55] M. Zhou, G. Xu, J. Tian, H. Hu und Q. Yuan, *Bainitic Transformation and Properties of Low Carbon Carbide-Free Bainitic Steels with Cr Addition,* Wuhan: MDPI, 2017.

[56] C. Garcia-Mateo, G. Paul, M. C. Somani, D. A. Porter, L. Bracke, A. Latz, C. Garcia De Andres und F. G. Caballero, *Perspective, Transferring Nanoscale Bainite Concept to Lower C Contents: A Perspective,* Metals, 2017.

[57] L. B. Timokhina, P. D. Hodgson und E. V. Pereloma, *Effect of Microstructure on the Stability of Retained Austenite in Transformation-Induced-Plasticity Steels,* METALLURGICAL AND MATERIALS TRANSACTIONS A, VOLUME 35A, AUGUST 2004— 2331, 2003.

[58] „Total Materia, Mais Detalhado Banco de Dados de Materiais do Mundo," Metals AG, April 2005. [Online]. Available: http://www.totalmateria.com/page.aspx?ID=CheckArticle&site=kts&LN=PT&NM=151. [Zugriff am 03 September 2017].

[59] F. M. Ashby und D. R. H. Jones, Engineering Materials 2: An Introduction to Microstructures, Processing and Design, Oxford: Elsevier, 1998.

[60] Saarstahl AG, „Saarstahl," Saarstahl AG, [Online]. Available: http://www.saarstahl.com/sag/de/produkte/stahl-loesungen/automotive/stahl-massivumformung/index.shtml. [Zugriff am 15 Juni 2017].

[61] S. Reisinger, G. Ressel, S. Eck und S. Marsoner, *Differentiation of grain orientation with corrosive and colour etching on a granular bainitic steel,* Elsevier Ltd, 2017.

[62] E. Weck und E. Leistner, Metallographic instructions for colour etching by immersion; Part I: Klemm colour etching, Düsseldorf: Deutscher Verlag für Schweißtechnik DVS - Verlag GmbH, 1995.

[63] *DIN 50125:2003-05: Testing of metallic materials - Tensile test pieces,* BEUTH.

[64] *DIN EN ISO 6892-1:2009-12: Metallic materials - Tensile testing - Part 1: Method of test at room temperature (ISO 6892-1:2009); German version EN ISO 6892-1:2009,* BEUTH.

[65] *ÖNORM EN ISO 6507-1: 2016 08 15: Metallische Werkstoffe - Härteprüfung nach Vickers - Teil 1: Prüfverfahren (ISO/DIS 6507-1:2016),* ON.

[66] *ASTM E 975 - 03(2008): Standard Practice for X-Ray Determination of Retained Austenite in Steel with Near Random Crystallographic Orientation,* ASTM.

[67] H. R. Ghazvinloo, A. Honarbakhsh-Raouf und E. Borhani, *MORPHOLOGICAL CHARACTERISTICS OF RETAINED AUSTENITE IN 0.362C–1.38Si–1.24Mn STEEL PROCESSED BY ONE-STEP QUENCHING AND PARTITIONING,* Semnan: Springer Science + Business Media New York, 2016.

[68] *DIN EN ISO 18265:2004-02: Metallische Werkstoffe - Umwertung von Härtewerten (ISO 18265:2003); Deutsche Fassung EN ISO 18265:2003,* BEUTH.